Doctoral Dissertation

Fabrication of Monoliths with Hierarchical Pores by Phase Separation and Their Applications

相分離法により構築される階層的多孔構造を有するモノリスの合成と応用

WANG YAN

June 2022

Graduate School of Engineering

Osaka University

Contents

General Introduction

Monoliths

In 1993, in the preparation of artificial sponge to separate proteins, monolith was first proposed by Noel *et al*. to represent a robust macroporous polymeric monolith. Since then, monolith have been used to represent single-piece bulk materials with a three-dimensionally connected porous or channel structure.

According to the nature of monolithic materials, monoliths were generally classified into three types containing organic monoliths, inorganic monoliths and organic-inorganic hybrid monoliths.[1-5] Among them, the organic monolith has the advantages of good biocompatibility and a wide pH range.[6-11] In particularly, its preparation process is very simple. Taking the fabrication process of monolithic capillary column as example (**Figure 1**), it is only required to mix monomer, crosslinker, initiator and porogenic solvent to form homongenous pre-polymerization solution, and then the solution is introduced into the capillary to fabricate organic monolithic column with porous structure by *in suit* polymerization. During the preparation process, the permeability and pore size of the prepared monoliths can be adjusted by changing the composition of pre-polymerization and reaction conditions, such as the ratio of porogenic solvent, the concentration of precusors and reaction temperature. Futhermore, a wide range of monomers is available for the preparation of organic monoliths. The different organic functional monomers can be used for different requirements in practical applications, while the surface of the monolith matrix can be modified or derived to show specific functions. However, organic monoliths also exhibit several disadvantages such as poor resistance to

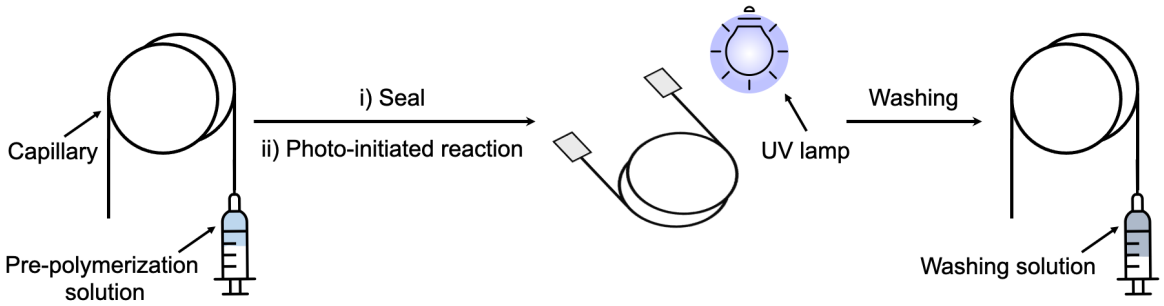

Figure 1. Schematic of the preparation of organic monolithic capillary column by photo-initiated reaction.

organic solvents, low mechanical strength and low thermal stability.[12] Compared with organic monoliths, inorganic monoliths have high mechanical strength and good resistance to organic solvents.[13, 14]Nevertheless, their preparation process is relatively tedious. For example, the fabrication of silica-based monoliths (**Figure 2**) usually requires hydrolysis, condensation, aging, ammonia treatment, drying, incineration and other steps, resulting a longer preparation cycle.[15] Simultaneously, inorganic monoliths have to undergo extra derivatization process to graft functional groups on their surface before they can be used in many fields. Because these steps in preparation process can cause damage the skeleton structure of the inorganic monoliths to varying degrees, the experimental conditions need to be strictly controlled. For organic-inorganic hybrid monoliths, they combined the advantages of both organic monoliths and silica monoliths, such as easy preparation process, stability performance, stable mechanical properties, and anti-swelling properties. Therefore, organic-inorganic hybrid monoliths have attracted the attention from scientists. At present, organic-inorganic hybrid monoliths with diverse functions can be synthesized *via* sol-gel reaction,[16] click reaction,[17] and ring-opening reaction[18] after choosing various commercial silane reagents (**Figure 3**), such as 3-(trimethoxysilyl)propyl methacrylate, glycidoxypropyltrimethoxysilane, vinyltrimethoxysilane, 3-

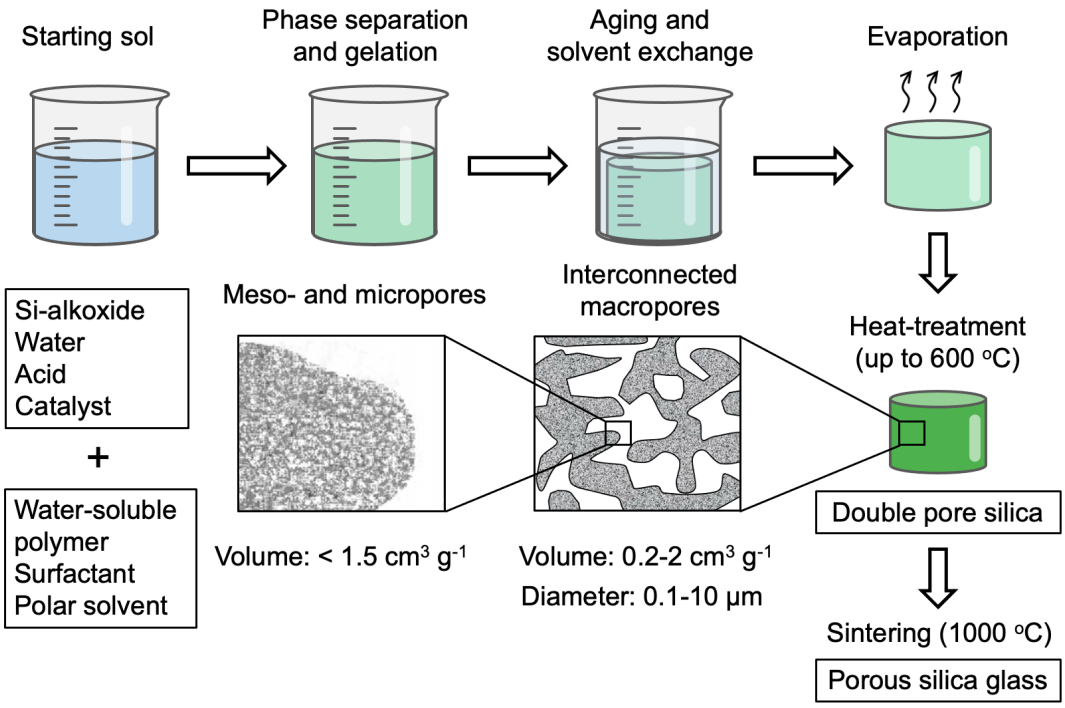

Figure 2. Schematic flow chart of the sample preparation procedure.[15]

mercaptopropyltrimethoxysilane, aminopropyltriethpxysilane, and 3-chloropropyltrimethoxysilane.[19]

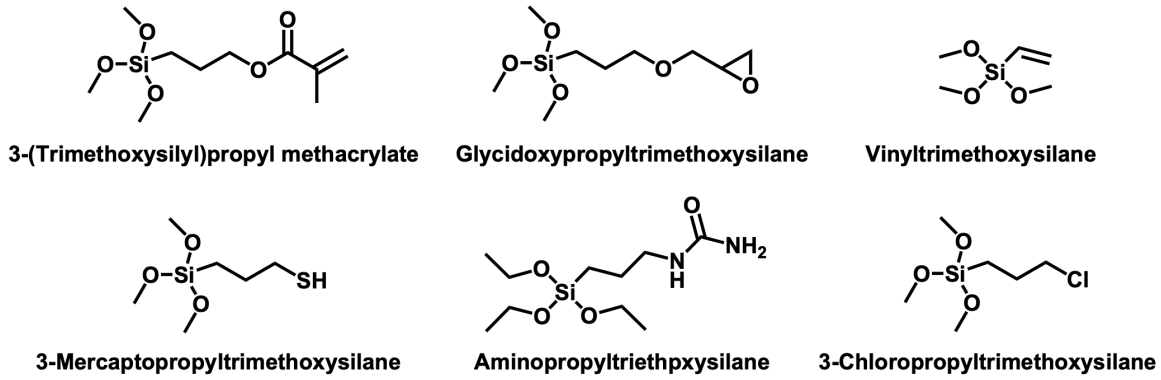

Figure 3. Chemical structures of organotrialkoxysilanes used for preparation of organic-inorganic hybrid monoliths.

Hierarchically porous structure

Hierarchically porous structures widely exist in nature from simple unicellular organisms to complex human tissue.[20, 21] The specific structure has attracted increasing attention by scientists, and thus diverse hierarchically porous materials have been fabricated.[22-24] Among these materials, hierarchically porous monolith (**Figure 4** and **5**) as a novel material simultaneously contains two or more pore scales, namely micropores (<2 nm), mesopores (2–50 nm), and macropores (>50 nm).[25-28] Micro- and mesopores can contribute to the generation of high surface areas and pore volumes, whichs provides size and shape selectivity and large interfacial areas. Meanwhile, macropores can reduce transport limitations and facilitate mass

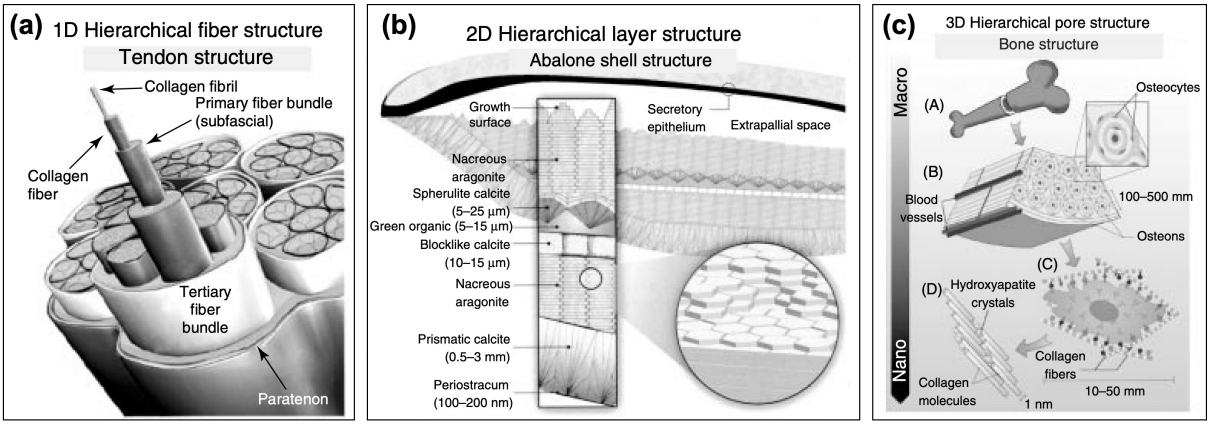

Figure 4. The classification of natural hierarchical structured materials: (a) hierarchical 1D fiber (tendon structure), (b) 2D layer (abalone shell structure), and (c) 3D pore (bone structure) structure.[25]

transport to the active sites. Moreover, they have three-dimensional continuous porous structure.[29-31] The fluid can pass through the materials, which avoided the disadvantages of powders and films. In the presences of properties containing easy fabrication process and efficient mass transfer and diffusion, hierarchically porous monoliths show broad application prospects in adsorption, separation, catalysis, and enrichment.[9, 32-39] For example, Ko *et al.* reported a facile strategy that is successfully used in the centimeter-scale preparation of hierarchically porous aminosilica monolith as a CO_2 adsorbent.[40] It was proved that the hierarchically porous structure improved properties over the single-mode porous component, with the macroporous framework ensuring mechanical stability and good mass transport properties, while the smaller pores provide the functionality for CO_2 adsorption.

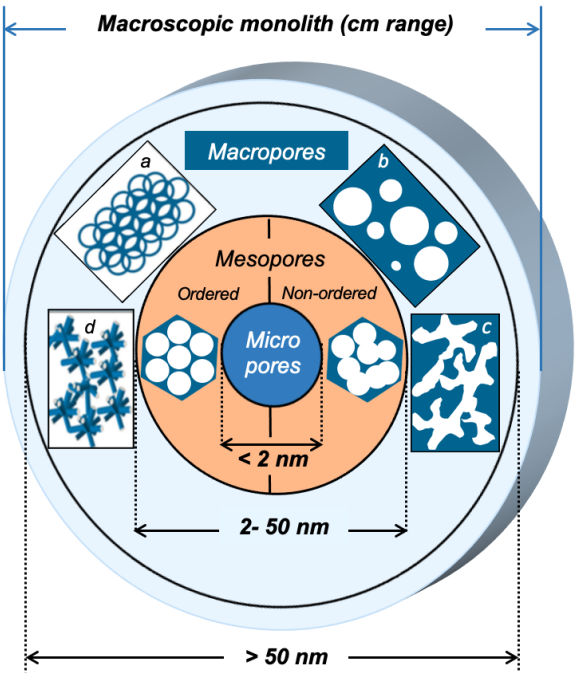

Figure 5. Concept of hierarchy in a porous material: schematics of a hierarchical porous build-up from the micrometer scale (inner blue circle), *via* the mesoscopic regime (orange circle) to the macroscopic porous dimension (light blue circle) within a monolithic material.[28]

Phase separation

Besides template method, emulsion method, and foaming method, phase separation is one of the most common approaches in the preparation of hierarchically porous monolith. The process of phase separation is a conversion from miscibility to immiscibility. By changing system conditions, the solubility of a certain component is reduced, and coagulates from the solution to form a new phase. Then, a porous structure could be generated when the solvent is removed. Common phase separation techniques mainly include thermally-induced phase separation (TIPS) and chemically-induced phase separation (CIPS). For TIPS, firstly, the polymer is completely dissolved in porogenic solvents to form homogenous solution at high temperature (above critical solution temperature). After the solution temperature is lower than

critical solution temperature, the precipitated phase will be generated to form two phases.10 For CIPS, in the initial phase, the monomers, crosslinker and initiator are dissolved in the porogenic solvents to form a homogeneous system. As the polymerization reaction proceeds, the molecular weight of the polymer continues to increase. The solubility in the solution containing the solvent and the remaining monomer decreases, which promotes the occurrence of phase separation. Then, the two phases gradually form which includes the solute phase (polymer-rich phase) and solvent phase (solvent-rich phase), while the two phases continue to grow as the phase separation process continues. When gel conversion occurs in the system, the solute phase constitutes the skeleton, and the positions are occupied by solvent phase can form mesoporous and macroporous structure. Subsequently, exchanging solvent occur on the skeleton surface of monolith using exchange solvent, and porous structure can further form on the surface skeleton, such as micropores.[41]

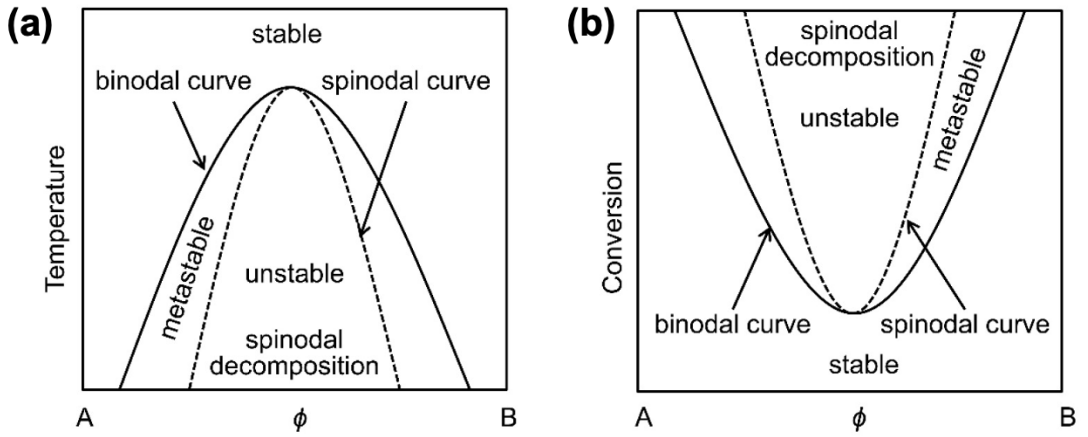

Figure 6. Schematic phase diagrams for (a) TIPS and (b) CIPS

Meanwhile, Flory–Huggins model can be employed to explain the occurrence formation of porous structure,[42-44] and the Gibbs energy (ΔG) of system is as follows:

$$\Delta G = -T\Delta S + \Delta H = RT(\frac{\phi_A}{P_A}\ln\phi A + \frac{\phi_B}{P_B}\ln\phi B + \chi_{AB}\phi_A\phi_B)$$

In this equation, R is thermodynamic constant; T is temperature of system; ϕ_A and ϕ_B are respectively volume fraction of components A and B; P_A and P_B are respectively degree of polymerization of components A and B; χ_{AB} is interaction parameter between A and B. When ΔG>0, the system changes from stable area to unstable area, and then phase separation occurs.

According to the above mentioned equation, it can be found that the decease of T, the decease of ΔS, and the increase of ΔH possibly lead to $\Delta G>0$, in which the decease of T is correspond with TIPS process (**Figure 6a**), and the decease of ΔS and the increase of ΔH are correspond with CIPS process (**Figure 6b**).[45] As shown in **Figure 6a**, with the reduction of temperature, the system enter the two-phase region from single-phase region, and become unstable to achieve phase separation. Likewise, with the formation of chemical bonds, the system enter the two-phase region to generate two phases. It can be seen that the conditions of phase separation have large influences on the formation of porous structure in monolith. For instance, the porogenic solvent mainly affects the solubility of the polymer, thereby affecting the time when phase separation occurs and the coarsening process of the solute phase in the later stage of phase separation. Generally, the higher the content of good solvent, the denser the pore structure and the smaller the pore size, and the effect of poor solvent is just the opposite. Thus, the different porous structure can be obtained by adjusting the porogenic solvents. On the other hand, when the reaction temperature is low, the conversion rate of the monomers is inhibited, and part of the resulting polymer is separated from the solvent phase, which may preferentially undergo nucleation and growth mechanism in the metastable region. The morphology of the formed polymer is granular or three-dimensional structures connected by approximately spherical particles. Increasing the temperature of the system can simultaneously increase the conversion rate of monomers and the solubility of polymers, thereby delaying the occurrence of phase separation, which is ultimately beneficial for the system to undergo a spinodal decomposition mechanism. At the later stage of phase separation, the coarsening process of the solute phase is suppressed, resulting in smaller pore sizes.

Design of hierarchically porous monolith in the dissertation

In the context, hierarchically porous monolith can be fabricated by chaning the conditions of phase separation, resulting diverse porous structure. Therefore, in this thesis, by investigate the conditions of phase separation, several hierarchically porous monoliths with good properties were synthesized *via* TIPS and CIPS. In Chapter 1, polyimide (PI)-based monoliths with great thermal stability and good mechanical strength were fabricated, thereby overcoming the

existing shortcomings of preparation of PI-based aerogels requiring complicated preparation processes and high cost. In Chapter 2, a flexible and highly efficient one-step synthesis was developed to fabricate hierarchically porous monolith using substituted acetylene and crosslinker in porogenic solvent *via* CIPS. The prepared monoliths showed good optical activity and large surface area, and thus exhibited good performance in enantioselective crystallization. In Chapter 3, to further develop the "one step" method in the preparation of monolith by helical polymer, the hierarchically porous boronic acid group-functionalized monoliths with optical activity were synthesized *via* CIPS, and showed potential in recognition, separation, and adsorption of compound with chirality and *cis*-diol groups.

Outline of this dissertation

In this dissertation, the author aimed at developing efficient methods for the prepararion of monoliths. By adjusting the conditions of phase separation, suitable hierarchically porous structure was formed in the monoliths, which could exert great potential in diverse appliacation. This doctoral dissertation is expected to provide universal route for the fabrication of other monolithic materials to broaden their field of application by means of displacing precursors.

Chapter 1

In this Chapter, two polyimide-based (PI-based) monoliths (pure PI monolith and hybrid PI monolith) with hierarchically porous structure were prepared using a cost-effective and facile method that avoids the shortcomings of traditional methods (**Scheme 1**). Through the introduction of octakis(glycidyldimethylsiloxy)octasilsesquioxane (POSS-epoxy) to the polyamic acid (PAA) prepared by 4,4'-oxydianiline (ODA) and pyromellitic dianhydride (PMDA), both hydrophobicity and mechanical strengths of the PI-based monoliths were improved. Moreover, the resulting PI-based monoliths exhibited suitable permeability, homogeneous morphology, and superior thermal stability. Adsorption tests demonstrated that the resulting hybrid PI monoliths exhibited better adsorption performance for organic solvents and silicone oil than pure PI monolith. Furthermore, the surface of polyhedral oligomeric silsesquioxane (POSS) hybridized PI (PI-*co*-POSS) monolith can be modified into a hydrophilic layer by reaction between the hydrophilic polymer and epoxy groups exposed on

the surface. This indicates that PI-*co*-POSS monoliths have potential in liquid diode application to achieve oil–water separation.

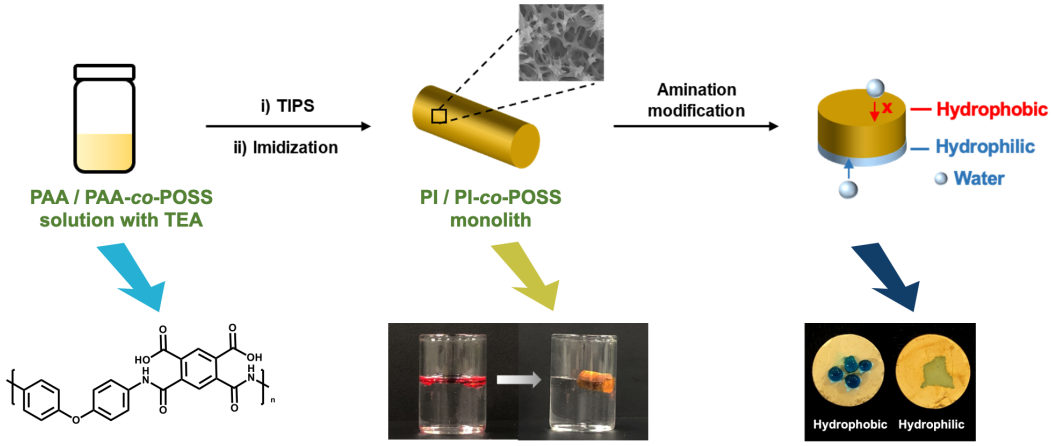

Scheme 1. Schematic of the preparation of PI-based monoliths.

Chapter 2

In this Chapter, a flexible and highly efficient one-step synthesis was developed to prepare chiral hierarchical porous monoliths *via* CIPS using substituted acetylene and crosslinker in the presence of porogenic solvent in which the complex doping and complicated procedures were not required (**Scheme 2**). It was demonstrated that hierarchical pore structure with through-pore and high surface area existed in the monoliths, which provides more chiral sites and space for interaction between monolithic materials and the solution. The porous structures and pore size can be adjusted by changing the conditions of phase separation. Moreover, the prepared monoliths exhibited good optical activity, thermal stability and mechanical properties. Therefore, the hierarchically porous monoliths with optical activity were applied in enantioselective crystallization and showed good performance.

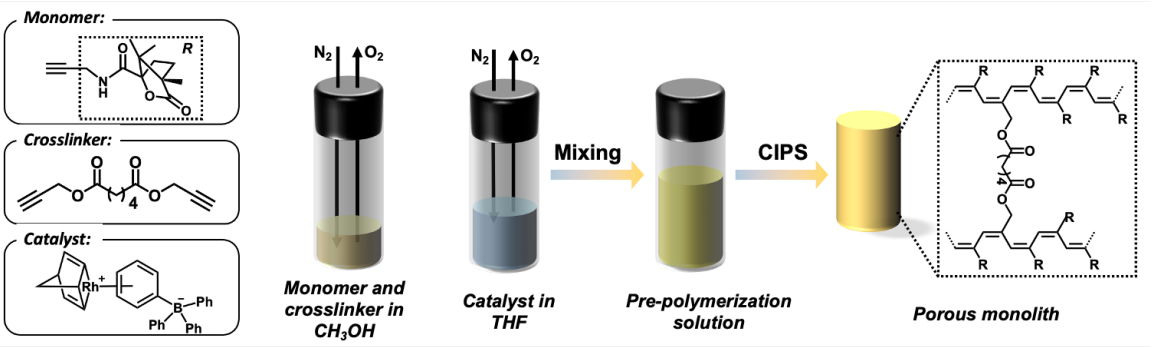

Scheme 2. Schematic of the preparation of chiral hierarchical porous monoliths.

Chapter 3

In this Chapter, hierarchically porous boronic acid group-functionalized monoliths that exhibited optical activity were fabricated with the facile "one step" method based on CIPS. Chiral substituted acetylene and achiral substituted acetylene with a boronic acid group were used as monomers (**Scheme 3**). By regulating the composition of the pre-polymerization solution, the permeability and macropore size of the porous structure could be controlled. In particular, the boronic acid functional group that can interact with a cis-diol group was successfully introduced on the skeleton surface of the monoliths. Further, the main chain of the copolymer that constituted the monoliths exhibited a high *cis* content and tacticity, and the monoliths showed good optical activity. Thus, the synthesize hierarchically porous boronic acid group-functionalized monoliths showed potential in recognition, separation, and adsorption of compound with chirality and *cis*-diol groups.

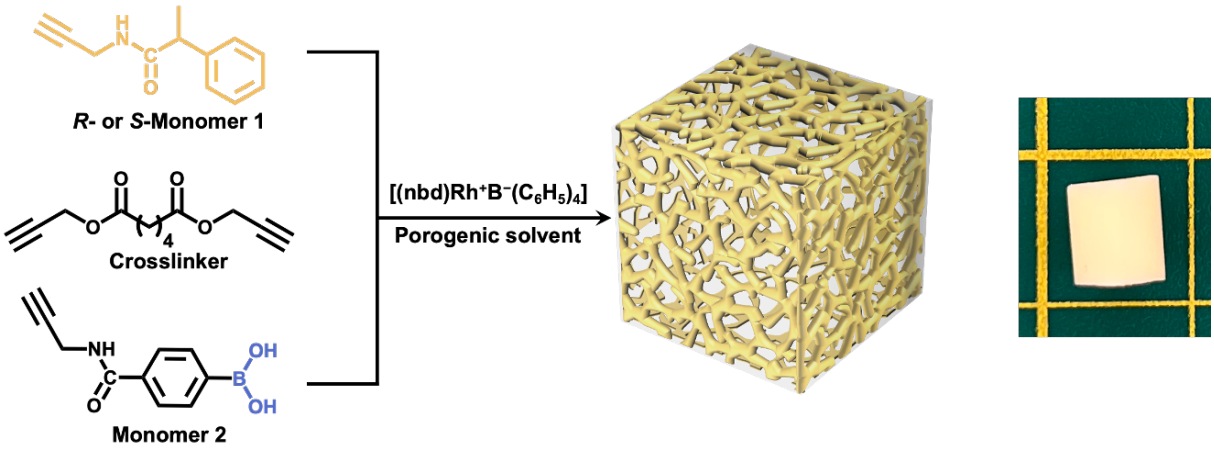

Scheme 3. Schematic of the preparation of hierarchically porous boronic acid group-functionalized monolith.

References

1. C. Acquah, C. K. S. Moy, M. K. Danquah, C. M. Ongkudon, *J. Chromatogr. B* 2016, **1015-1016**, 121–134.
2. H. Minakuchi, K. Nakanishi, N. Soga, N. Ishizuka, N.Tanaka, *J. Chromatogr. A* 1994, **762**, 135–146.
3. S. Hjertén, J. Liao, R. Zhang, *J. Chromatogr. A* 1989, **473**, 273–275.
4. F. Svec, J. M. J. Fréchet, *J. Chromatogr. A* 1995, **702**, 98–95.
5. T.B. Tennikova, M. Bleha, F. Švec, T.V. Almazova, B. G. Belenkii, *J. Chromatogr. A* 1991, **555**, 97–107.
6. Q. Wang, H. Wu, K. Peng, H. Jin, H. Shao, Y. Wang, J. Crommen, Z. Jiang, *Anal. Chim. Acta* 2018, **999**, 184–189.
7. L. Ren, Z. Liu, Y. Liu, P. Dou, H.-Y. Chen, *Angew. Chem. Int. Ed.* 2009, **121**, 6832–6835.
8. J. Liu, M. Li, P. Wang, K. Liu, Y. Fang, *Chem. Eng. J.* 2018, **339**, 14–21.
9. H. Lin, J. Ou, Z. Liu, H. Wang, J. Dong, H. Zou, *Anal. Chem.* 2015, **87**, 3476–3483.
10. Y. Li, M. L. Lee, *J. Sep. Sci.* 2009, **32**, 3369–3378.
11. J. Bai, J. Ou, H. Zhang, S. Ma, Y. Shen, M. Ye, *J. Chromatogr. A* 2017, **1514**, 72–79.
12. R. J. Groarke, D. Brabazon, *Materials* 2016, **9**, 446.
13. Z. Walsh, B. Paull, M. Macka, *Anal. Chim. Acta* 2012, **750**, 28–47.
14. N. Ishizuka, H. Minakuchi, K. Nakanishi, N. Soga, N.Tanaka, *J. Chromatogr. A* 1998, **797**, 133–137.
15. K. Nakanishi, H. Minakuchi, N. Soga, N. Tanaka, *J. Solgel Sci. Technol.* 1998, **13**, 163–169.
16. Z. Zajickova, *J. Sep. Sci.* 2017, **40**, 25–48.
17. Z. Liu, J. Ou, H. Zou, *TrAC, Trends Anal. Chem.* 2016, **82**, 89–99.
18. H. Wang, J. Ou, H. Lin, Z. Liu, G. Huang, J. Dong, H. Zou, *J. Chromatogr. A* 2014, **1367**, 131–140.
19. H. Colon, X. Zhang, J. K. Murphy, J. G. Rivera, L. A. Colon, *Chem. Commun.* 2005, 22,

2826–2828.

20. X. Y. Yang, L. H. Chen, Y. Li, J. C. Rooke, C. Sanchez, B. L. Su, *Chem. Soc. Rev.* 2017, **46**, 481–558.
21. M. H. Sun, S. Z. Huang, L. H. Chen, Y. Li, X. Y. Yang, Z. Y. Yuan, B. L. Su, *Chem. Soc. Rev.* 2016, **45**, 3479–3563.
22. X. Peng, L. Zhang, Z. Chen, L. Zhong, D. Zhao, X. Chi, X. Zhao, L. Li, X. Lu, K. Leng, C. Liu, W. Liu, W. Tang, K. P. Loh, *Adv. Mater.* 2019, **31**, e1900341.
23. M. Sun, C. Chen, L. Chen, B. Su, *Front. Chem. Sci. Eng.* 2016, **10**, 301–347.
24. L. Wu, C. Zhou, B. Zhang, H. Lei, W. Wang, X. Pu, L. Liu, J. Liang, Y. Fan, X. Zhang, *ACS Appl. Mater. Interfaces* 2020, **12**, 48395–48407.
25. B. Su, C. Sanchez, X. Yang, *Hierarchically structured porous materials*, 2011, 3–27.
26. C. M. Parlett, K. Wilson, A. F. Lee, *Chem. Soc. Rev.* 2013, **42**, 3876–3893.
27. I. Nischang, T. J. Causon, *TrAC, Trends Anal. Chem.* 2016, **75**, 108–117.
28. A. Feinle, M. S. Elsaesser, N. Husing, *Chem. Soc. Rev.* 2016, **45**, 3377–3399.
29. Y. S. Hu, P. Adelhelm, B. M. Smarsly, S. Hore, M. Antonietti, J. Maier, *Adv. Funct. Mater.* 2007, **17**, 1873–1878.
30. S. Song, J. Torkelson, *Macromolecules* 1994, **27**, 6389–6397.
31. L. Zhang, Y. Wang, L. Pan, R. Tang, T.-A. Asoh, J. Ou, H. Uyama, *Green Chem.* 2021, **23**, 7674–7684.
32. C. Triantafillidis, M. S. Elsaesser, N. Husing, *Chem. Soc. Rev.* 2013, **42**, 3833–3846.
33. Y. Mi, W. Zhou, Q. Li, D. Zhang, R. Zhang, G. Ma, Z. Su, *RSC Adv.* 2015, **5**, 55419–55427.
34. F. Lorignon, A. Gossard, M. Carboni, *Chem. Eng. J.* 2020, **393**.
35. Y. Li, Z. Zhang, B. Ge, X. Men, Q. Xue, *Green Chem.* 2016, **18**, 5266–5272.
36. H. Li, D. Yuan, C. Tang, S. Wang, J. Sun, Z. Li, T. Tang, F. Wang, H. Gong, C. He, *Carbon* 2016, **100**, 151–157.
37. A. Inayat, B. Reinhardt, H. Uhlig, W. D. Einicke, D. Enke, *Chem. Soc. Rev.* 2013, **42**, 3753–3764.
38. L. Z. Fan, Y. S. Hu, J. Maier, P. Adelhelm, B. Smarsly, M. Antonietti, *Adv. Funct. Mater.*

2007, **17**, 3083–3087.

39. C. Chen, S. T. Yang, W. S. Ahn, R. Ryoo, *Chem. Commun.* 2009, **24**, 3627–3629.
40. Y. G. Ko, H. J. Lee, J. Y. Kim, U. S. Choi, *ACS Appl. Mater. Interfaces* 2014, **6**, 12988–12996.
41. Z. T. Xie, T. A. Asoh, H. Uyama, *Carbohydr. Polym.* 2019, **214**, 195–203.
42. Joachim Kiefer, James L. Hedrick, J. G. Hilborn, *Macromolecular Architectures*, 1999, **147**, 161–247.
43. M. L. Huggins, *J. Am. Chem. Soc.* 1942, **664**, 2716–2718.
44. P. J. Flory, *J. Chem. Phys.* 1942, **10**, 51–61.
45. K. Nakanishi, *J. Porous Mater.* 1997, **4**, 67–112.

Chapter 1.

Hydrophobic and hydrophilic modification of hierarchically porous monolithic polyimide derivatives as functional liquid absorbers

1.1 Introduction

Since Bogert and Renshaw synthesized aromatic PI by the self-condensation polymerization of 4-amino-*o*-phthalic acid in 1908, interest in PIs has been growing steadily owing to their thermo-oxidative stability, unique electrical properties, high radiation and solvent resistance, and high mechanical strength.[1-4] For example, PI materials including films and aerogels have been widely applied in a wide range of fields such as semiconductor fabrication[5], microelectronics[6], gas storage[7], and separation[8].

Among various materials, polymer monolith as a porous material exhibit many advantages including chemical stability, selectivity, ease of modification and mechanical stability.[9-11] Because of these characteristics, they are widely applied in adsorption[12, 13], catalysis[14, 15], energy storage[16, 17], and separation fields[18, 19]. Therefore, various porous PIs have been reported,[20-22] and PI monoliths that enable further functionalization such as improvement of heat resistance, hydrophobicity, and surface modification ability are required for a wide range of applications in the future.

Polyhedral oligomeric silsesquioxane (POSS) with a cage-like structure is an organic–inorganic hybrid molecule of nanoscale size (1–3 nm). It can be introduced into a reaction system to prepare monolithic materials with good performance because it exhibits distinctive properties, such as thermal performance, dielectric performance, and small-size and macroscopic quantum effects. The skeleton of the POSS molecule is composed of Si–O–Si structural units that endows it with chemical inertness and thermostability. Moreover, there are various substituted POSS reagents containing one or more alkyl, vinyl, epoxy, carboxyl, and methacryloyloxy functional groups. These reactive groups offer reactivity for POSS reagents, which increases the compatibility of POSS with other molecules and polymers. Therefore, the incorporation of POSS reagents into a reaction system not only improves the chemical and

physical properties of the polymer but also allows the remaining reactive functional groups to be used to achieve further surface modifications. Therefore, it is necessary to newly design a porous material consisting of PI and POSS.

In this study, the author prepared a POSS hybridized PI (PI-*co*-POSS) monolith with a co-continuous porous structure. PI and PI-*co*-POSS monoliths exhibit a hierarchical porous structure, and the introduction of POSS improves mechanical strength. Because the PI-*co*-POSS monolith has improved hydrophobicity compared to the PI monolith, it exhibits excellent organic solvent and silicone oil absorption capacity. Furthermore, we found that the surface of PI-*co*-POSS monolith can be modified into a hydrophilic layer by reaction between the hydrophilic polymer and epoxy groups exposed on the surface. The overall design, including the chemical composition, skeleton, and surface, can be an innovation in porous PI for application in various fields.

1.2 Experimental Section

1.2.1 Materials

PMDA (≥98%) and ODA (≥98%) were obtained from Tokyo Chemical Industry Co., Ltd. (Japan). POSS-epoxy was purchased from Sigma (USA). The deionized water used in all the experiments was purified with a Milli-Q system (Millipore, Inc., USA). Super dehydrated DMF (99.5%) and branched polyethylenimine (bPEI, an average molecular weight of ~600) were purchased from FUJIFILM Wako Pure Chemical Corp. (Japan). Toluene, TEA, and DMF were purchased from Nacalai Tesque, Inc. (Japan). All reagents were used as received.

1.2.2 Preparation of PI monolith

Generally, the preparation of PAA is the first step of synthesis method of PI. To synthesize PAA, ODA (10.4 mol, 2.07 g) was first dissolved in super dehydrated DMF (15.0 mL), and then 10.0 mmol PMDA (2.00 g) was added into the above solution under a nitrogen atmosphere which was followed by magnetic stirring at room temperature for 24 h. The prepared PAA solution was transferred into a glass bottle and stirred at 85 °C until its temperature reached equilibrium. Deionized water and TEA were then added dropwise into the PAA solution, and the mixture was heated at 85 °C until it became a yellow and transparent solution. The mixture was then transformed into a 25 °C water bath for 12 h and became an opaque yellow hydrogel. Subsequently, 50% DMF in H_2O, 25% DMF in H_2O, and 100% H_2O in sequence were selected as exchange solvents. The product was then dried by vacuum drying for 4 h at ambient temperature to obtain PAA monolith. Finally, PAA monolith was converted to PI monolith. The detailed procedure was as follows: PAA monolith was placed in an oven with temperature programming (80 °C for 2 h, 120 °C for 1 h, 150 °C for 1 h, 180 °C for 2 h, 250 °C for 1 h, and 280 °C for 2 h in proper order). After the temperature of the oven was reduced below 50 °C, the PI monolith can be obtained.

1.2.3 Preparation of PI-*co*-POSS monolith

The 10.4 mmol ODA (2.07 g) was completely dissolved in DMF (13 mL) under a nitrogen

atmosphere in an ice bath, then 10.0 mmol PMDA (2.00 g) was added to the solution under stirring at room temperature for 1 h. Subsequently, a solution of 0.19 or 0.39 g POSS-epoxy dissolved in 2 mL super dehydrated DMF was added dropwise to react for 24 h. The resulting solution is the precursor material for the monolithic PI-*co*-POSS materials. The other preparation processes for PI-*co*-POSS monolith are the same as those for PI monolith.

1.2.4 Surface modification of PI-*co*-POSS monolith

A certain mass of bPEI was dissolved in ethanol to prepare the bPEI–ethanol solution (30%, v/v). Then, a portion of the PI-*co*-POSS monolith was immersed in the solution to react for 24 h at 50 °C. Finally, the modified PI-*co*-POSS monolith was dried by vacuum drying after unreacted bPEI was washed away with ethanol.

1.2.5 Determination of absorption capacity

Different organic solvents (tetrahydrofuran, hexane, DMF, acetic acid, chloroform, toluene, and 2-propanol) and silicone oil were adopted to measure the absorption capacities of the resulting monoliths. Each weighed monolith was immersed in a certain solvent and placed in a shaker. After 10 min, the monolith was removed from the solvent, wiped dry, and weighed again to obtain its mass. The mass difference before and after adsorption divided by the mass before adsorption was used to calculate the adsorption capacity of the monolith.

1.2.6 Instruments and methods

The microstructure and pore morphology of the monolithic materials were observed by scanning electron microscopy (SEM) (Hitachi SU-3500, Japan). The attenuated total reflection infrared (ATR-IR) spectra were determined on a spectrometer (Thermo Scientific Nicolet iS5, Japan) equipped with an iD5 ATR attachment. Thermogravimetric analysis (TGA) curves were recorded using a thermogravimetric analyzer (Hitachi STA7200RV, Japan) by heating from 40 to 1000 °C under nitrogen protection. The water contact angle was obtained on a Drop Master DM300 (Kyowa Interface Science, Japan) with 1.0-μL water drops. The compression performance of the materials was measured by using a universal testing machine (Shimadzu EZ Graph, Japan) with a compression speed of 1 mm/min. The maximum compression strain (ε)

was set to 70%. The Brunauer–Emmett–Teller (BET) surface area was evaluated by using a nitrogen adsorption–desorption analyzer (Quantachrome Instruments, USA). The pore diameter distribution and pore volume were acquired using density functional theory (DFT).

From Darcy's law, the permeability of the resulting monoliths can be calculated according to the equation $B_0 = F\eta L/(\pi r^2 \Delta P)$, in which F (m^3 s^{-1}) is the flow rate of the mobile phase, η (Pa s) is the viscosity of the mobile phase (0.89×10^{-3} Pa s for water), L (m) and r (m) are the effective length and inner diameter of the column, respectively, and ΔP (Pa) is the pressure drop across the monolith.[30] The ΔP data were measured with a digital pressure gauge (Krone KDM30, Japan). The flow rates were controlled by using a digital quantitative tubing pump (As One DSP-100SA, Japan).

1.3 Results and discussion

1.3.1 Preparation of monolithic PI and PI-*co*-POSS materials

Porous materials can generally be prepared in various ways including phase separation[23], hard template method[24], foaming method[25], and the emulsion method[26]. For phase separation, thermally induced phase separation (TIPS) and chemically induced phase separation (CIPS), system conditions are changed to reduce the solubility of certain components that led to the aggregation of a new phase from the polymerization solution. When the solvents were removed, the porous monolith was successfully fabricated. In this case, TIPS approach was applied in the fabrication of porous monolithic polyamic acid-based (PAA-based) materials for the first time. Furthermore, both thermal and chemical methods are usually used to prepare PI. Because the solvent used in the chemical method can destroy the structure of PAA monolith, the thermal method was chosen to achieve imidization in this study. PI-based monoliths were prepared according to the process shown in **Schemes 1-1 and 1-2a**.

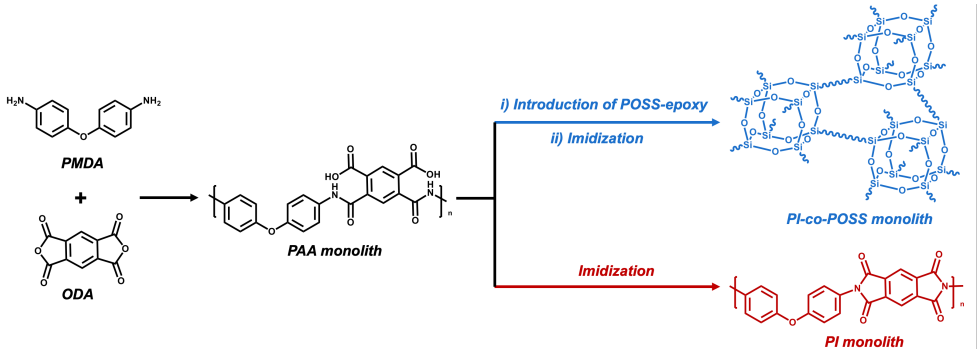

Scheme 1-1. The preparation processes of PI and PI-*co*-POSS monoliths.

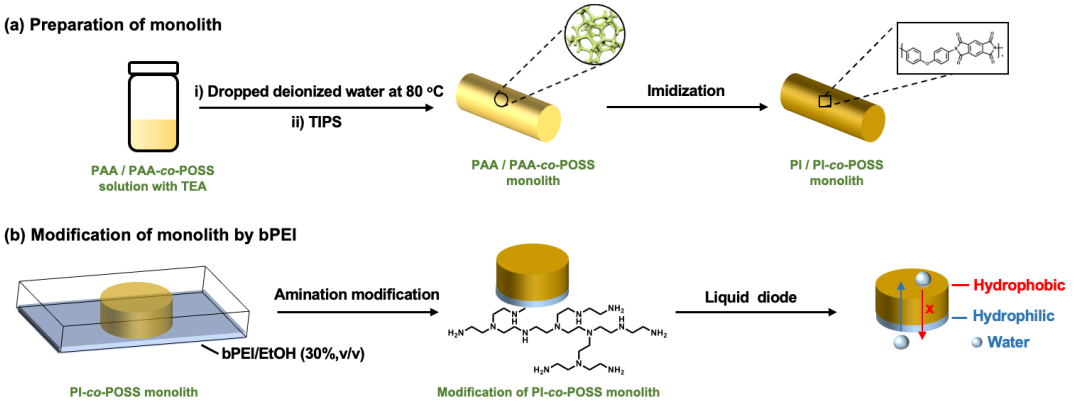

Scheme 1-2. (a) Preparation of PI/PI-*co*-POSS monoliths *via* TIPS and thermal imidization. (b) Modification

of PI-*co*-POSS monolith by bPEI.

The solvent is one of the most important factors affecting the formation of the pore structure and skeleton of the polymeric monolith during phase separation. The PAA solution as a predecessor was synthesized using PMDA and ODA and evenly dissolved in super dehydrated *N,N*-dimethylformamide (DMF). In the context, DMF was chosen as a good solvent, having a high boiling point and being suitable for TIPS during heating. To select a poor solvent, PAA solution was dropped into various solvent containing acetone, methanol, ethanol, and deionized water, respectively. Finally, the mixture of DMF and deionized water was chosen as porogenic solvent for phase separation, because the PAA solution (with DMF as the solvent) could be precipitated immediately in deionized water. The composition of the PAA solution before phase separation is listed in **Table 1-1**. The effect of solvent proportion in monolith formation was investigated first. As presented in **Table 1-1**, when the weight percentage of DMF in the mixture was 58.8%, the PAA solution was precipitated in the solvent, and not homogenous even at 80 °C with stirring for long time and cannot form monolith at low temperature. With increasing DMF content (64.5%), the PAA solution could form monolith 2 by phase separation at 25 °C. However, as the content of DMF rose to 70.6%, phase separation did not occur even at a quite low temperature. This phenomenon illustrated DMF as good solvent and water as poor solvent. Subsequently, the pore morphology of monolith 2 was characterized by SEM, it exhibited a globular and discontinuous pore structure (**Figure 1-1a**). To obtain a continuous porous structure and a number of through-pores in the monolith, TEA was introduced into the solvent system. Therefore, different amounts of TEA were added to the PAA solution to investigate its influence on the PI monolith. When the amount of TEA was kept at 50 μL, phase separation successfully occurred and the permeability of monolith 4 was 1.03×10^{-14} m^2. However, the monolith could not form when the TEA content rose to 100 μL. This was due to the generation of some PAA ammonium salt, which increased the solubility of the polymers in water. Although the PAA solution could undergo phase separation when more deionized water was dropped, the resulting monolith was too soft and easily broken while exchanging solvents. Moreover, a comparison of the SEM images of monoliths 2 (**Figure 1-1a**) and 4 **(Figure 1-1b**) shows that

the globular and discontinuous pore structure disappeared and through-pores appeared in monolith 2. Because the mechanism of phase separation might be changed by the addition of TEA.[27]

Table 1-1. Detailed composition of polymerization mixtures, cooling temperature, and permeability of monoliths.

Monolith[a]	POSS-epoxy[b] (wt%)	Monomer concentration (mg mL^{-1})	DMF[c] (wt%)	H_2O[c] (wt%)	TEA (μL)	Cooling temperature (°C)	Permeability ($\times10^{-14}$ m^2)
1	0	182.9	58.8	41.2	0	25	—[d]
2	0	182.9	64.5	35.4	0	25	—[f]
3	0	182.9	70.6	19.4	0	25	—[e]
4	0	182.9	64.5	35.4	50	25	1.03
5	0	182.9	64.5	35.4	100	25	—[d]
6	0	182.9	64.5	35.4	50	4	0.82
7	0	182.9	64.5	35.4	50	50	—[d]
8	0	166.7	64.5	35.4	50	25	2.33
9	0	149.2	64.5	35.4	50	25	—[d]
10	3.7	173.2	64.5	35.4	0	25	—[f]
11	3.7	173.2	64.5	35.4	50	25	4.01
12	3.7	173.2	64.5	35.4	100	25	—[d]
13	7.1	179.6	64.5	35.4	0	25	—[f]
14	7.1	179.6	64.5	35.4	50	25	3.85
15	7.1	179.6	64.5	35.4	100	25	—[d]

[a] The prepolymerization solution also contained 138.1 mg of the monomer ODA and 145.4 mg of PMDA.

[b] Weight percentage of POSS-epoxy in total monomers.

[c] Weight percentage of solvent in the porogenic system mixture.

[d] The prepolymerization solution cannot form monoliths.

[e] The prepolymerization solution was not homogeneous.

[f] The monolith did not possess through-pores.

Subsequently, three monoliths were synthesized at different temperatures for phase separation while keeping other experimental conditions the same (monoliths 4, 6, and 7 in **Table 1-1**). When the cooling temperature was set to 4 °C, it can be clearly observed that phase separation occurred in 20 s during the fabrication process of monolith 6. For monolith 4, phase separation gradually emerged within 2 min. When the cooling temperature was kept at 50 °C, the monolith cannot form because of the evaporation of poor solvent and extremely slow speed of phase separation. These phenomena demonstrate that the speed of phase separation process

was quite fast at lower temperature. In addition, SEM images (**Figure 1-1b** and **c**) provided illustrative insight into the impact of the cooling temperature on the morphologies of the two monoliths (monoliths 4 and 6). The pore size of monolith 6 was smaller and its skeleton was thinner compared with those of monolith 4, while the permeability of monolith 6 was 0.82 × 10^{-14} m^2 and lower than monolith 4. Meanwhile, there is no obvious pore structure in monolith 7 (**Figure 1-1d**). These results illustrate that the lower cooling temperature can endow the monolith with a thinner skeletal structure and smaller pore size because of the high speed of phase separation and that the pore size of the monoliths can be scaled by adjusting the cooling temperature. Monomer concentration also plays an important role in the formation of monolith. Therefore, the effect of different concentrations was investigated, and the results are listed in **Table 1-1**. When the concentration decreased from 182.9 to 166.7 mg mL^{-1}, the permeability increased from 1.03 to 2.33 × 10^{-14} m^2. Corresponding with these permeability results, both pore size and skeleton density of monolith decreased with decreasing monomer concentration (**Figures 1-1** and **1-3d**), while there is no homogenous pore structure in monolith 9 (**Figure 1-1e**) because of the lower concentration (149.2 mg mL^{-1}).

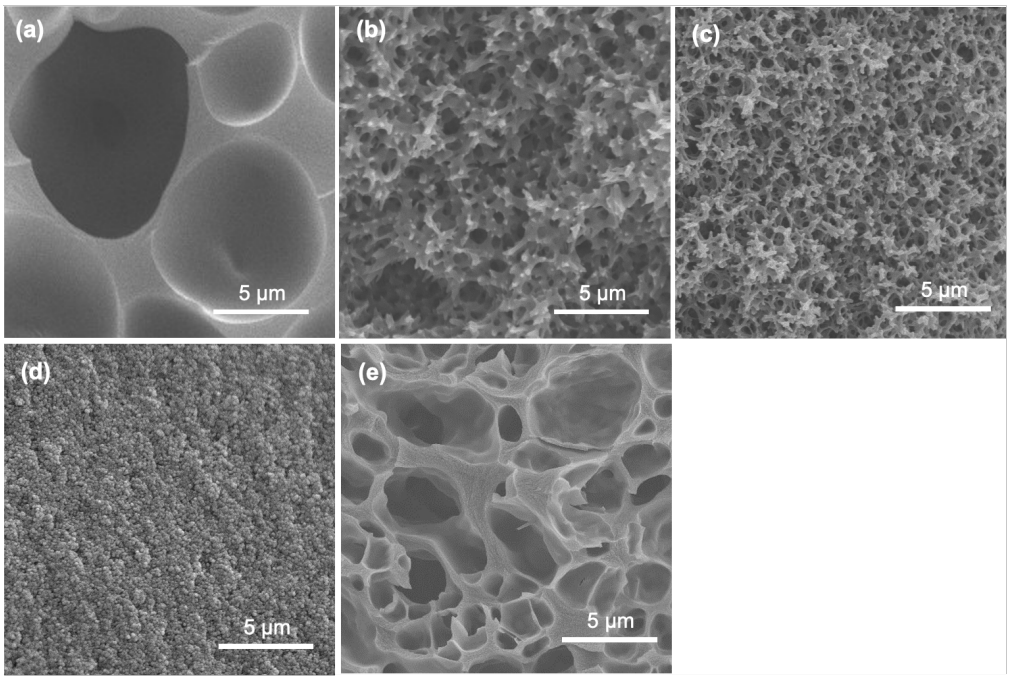

Figure 1-1. SEM images of (a) monolith 2, (b) monolith 4, (c) monolith 6, (d) monolith 7, and (e) monolith 9 at 5000× magnification.

According to the ratio of ODA to PMDA, it can be observed that excess amine groups were exposed on the ends of PAA. These amine groups can react with epoxy groups in POSS-epoxy (crosslinker) to introduce some epoxy groups, enabling the resulting PI-*co*-POSS monolith to be easily modified. As given in **Table 1-1**, the ratios of epoxy and terminal amine groups were, respectively, set to 1/1 (monolith 11) and 1/2 (monolith 14) to investigate the influence of the amount of POSS-epoxy. Upon increasing the POSS-epoxy content in total monomers from 0 to 7.1%, the permeabilities of monolith 11 and 14 respectively increased to 4.01×10^{-14} and 3.85×10^{-14} m^2. This result can be attributed to loose structure of PI-*co*-POSS monolith, resulting from the existence of the tough silsesquioxane cores and large network.[28] Based on the above results (suitable permeability and porous morphology), monoliths 8, 11, and 14 were chosen for additional characterization and application in the following experiments.

1.3.2 Characterization of PI and PI-*co*-POSS monolith

In this study, the PAA monolith was first fabricated, and then the thermal method was used to perform imidization to form PI monolith. ATR-IR spectra were used to confirm the transformation from PAA (the predecessor of monolith 8) to PI (monolith 8). As shown in **Figure 1-2**, the characteristic peaks of the carboxyl group appeared at 3400–2200 cm^{-1} (**Figure 1-2a**), while these signals disappeared in the spectrum of PI monolith (**Figure 1-2b**). More importantly, the characteristic absorption peaks at 1776, 1720, and 752 cm^{-1} were assigned as symmetrical and asymmetrical stretching vibrations and the bending vibration of the imide ring, respectively (**Figure 1-2b**), confirming the existence of an aromatic imide structure. The signals of Si–O–Si stretching at 1089 and 799 cm^{-1} and the peaks of epoxy group at 909 cm^{-1} observed in **Figure 1-2c** indicate

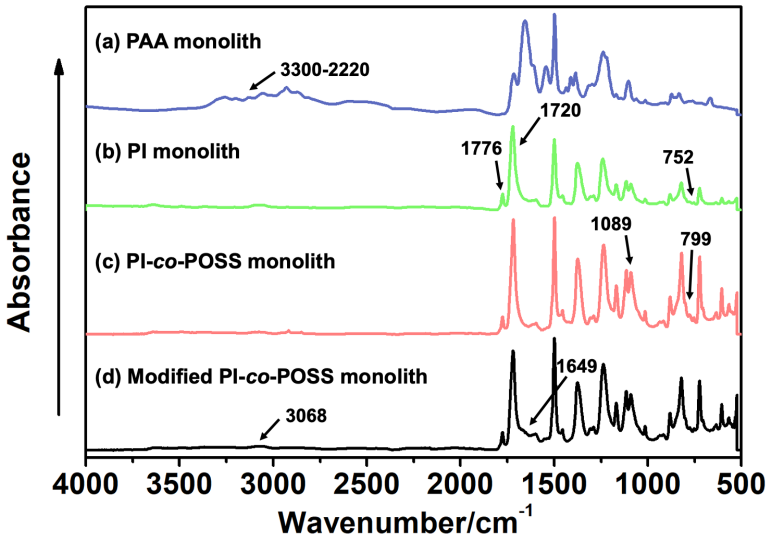

Figure 1-2. ATR-IR spectra of (a) PAA (the predecessor of monolith 8), (b) PI (monolith 8), and (c) PI-*co*-POSS (monolith 14) monoliths.

that the POSS reagent was successfully introduced into reaction system, and the epoxy groups were stable after imidization. These results demonstrate that POSS-epoxy successfully reacted with the amine group exposed at the ends of PAA and was introduced into the system.

To confirm the transformation of porous morphology between PAA and PI monolith, SEM was employed. **Figures 1-3a** and **d** show images of an interconnected network structure with pore size focused on ~2 μm. The morphology of PI monolith was almost maintained after the thermal imidization. Moreover, to verify the influence of the amount of POSS-epoxy in the microstructure, PI and PI-*co*-POSS monoliths were also characterized by SEM. Likewise, there was no obvious difference between porous structure of PAA-*co*-POSS and PI-*co*-POSS monoliths, indicating that porous structure was not influenced by imidization. In addition, as can be seen in **Figures 1-3d–f**, both PI (monolith 8) and PI-*co*-POSS (monoliths 11 and 14) have homogeneous network structure and through-pore. Comparison of the SEM imagines of PI (**Figure 1-3d**) and PI-*co*-POSS (**Figures 1-3e** and **f**) monoliths distinctly shows that the skeleton of the monolith became thinner when the POSS-epoxy was added to the polymerization. The porous structure was obviously favorable for fluid flow and mass exchange on the monolith. In addition, the pore size distributions and specific surface areas of PI and PI-*co*-POSS monoliths were investigated by measuring nitrogen gas (N_2) adsorption–desorption at 77 K, as shown in **Figure 1-4**. It can be observed from the pore size distribution in **Figure 1-4b** that micro- and mesopores also existed in the three monoliths. Combined with the SEM images, these results indicate that the PI and PI-*co*-POSS monoliths exhibit a hierarchically porous structure including micropores, mesopores, and macropores. Meanwhile, the surface areas of the three monoliths are, respectively, 7.05, 17.04, and 17.52 $m^2\ g^{-1}$. These variations are attributed to the varying amounts of micro- and mesopores.

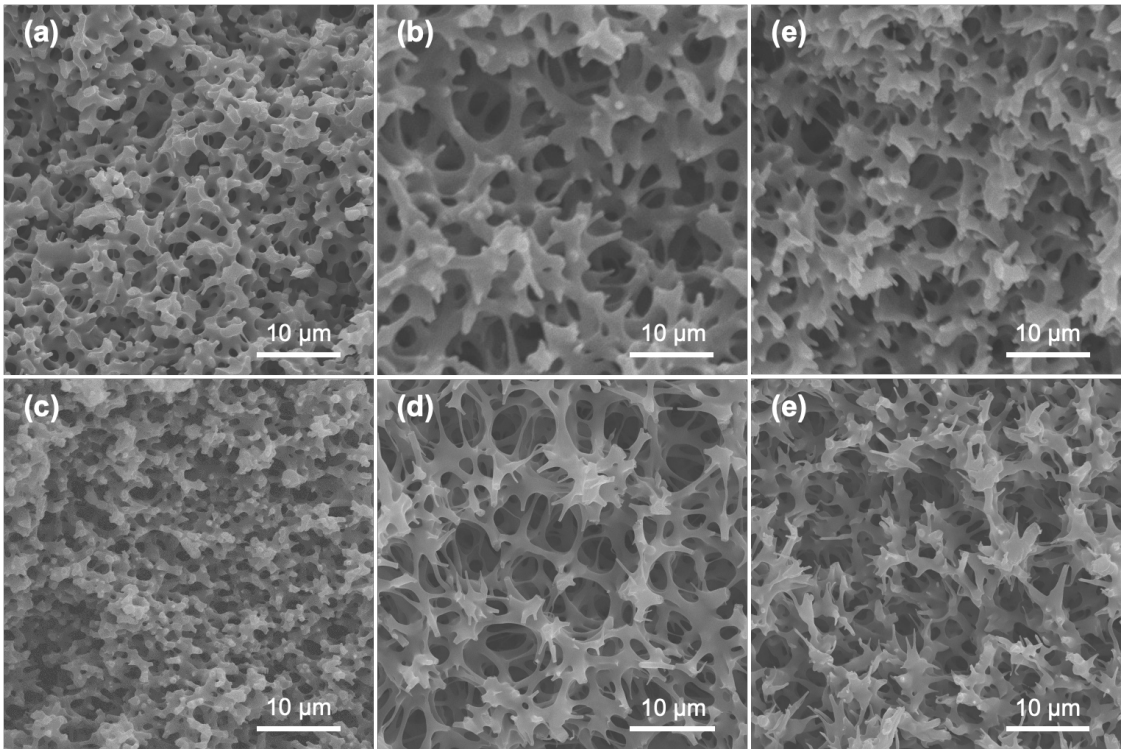

Figure 1-3. 2000 × magnified SEM images of (a) PAA monolith (the predecessor of monolith 8), PAA-*co*-POSS monoliths for the predecessors of (b) monolith 11 and (c) monolith 14, (d) pure PI monolith (monolith 8) and PI-*co*-POSS monoliths for (e) monolith 11 and (f) monolith 14.

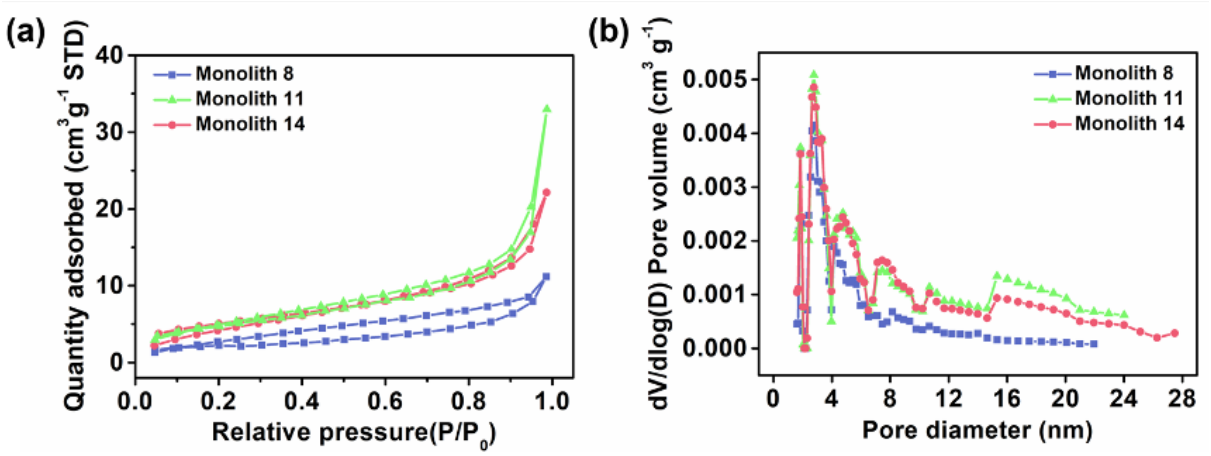

Figure 1-4. Nitrogen adsorption–desorption isotherms of (a) monolith 8, monolith 11, and monolith 14 and corresponding pore size distribution plots of (b) monolith 8, monolith 11, and monolith 14.

To evaluate the thermal stability of the PI and PI-*co*-POSS monoliths, TGA was adopted to test these samples under a nitrogen atmosphere. One can observe in **Figure 1-5a** that the pure PI monolith lost its weight from 555 °C, while the weight loss of the two PI-*co*-POSS monoliths apparently occurred from 539 and 534 °C, respectively. Comparison of the TGA curves of PI

with those of PI-*co*-POSS monoliths reveals a slight decrease in decomposition temperature appearing in PI-*co*-POSS monoliths, because the organic section of POSS-epoxy exhibited a lower degradation temperature. The TGA diagrams demonstrate that the PI and PI-*co*-POSS monoliths have great thermal stability and that ring-opening polymerization successfully occurred between the epoxy group in POSS-epoxy and the amino group in pure PAA because of the difference of residual weight. In the completely dried state, PI and PI-*co*-POSS monoliths were characterized by compression testing to investigate and compare their mechanical strength (**Figure 1-5b**). Compression tests were implemented by compressing cylindrically shaped PI and PI-*co*-POSS monoliths from 0 to 500 N, as shown in **Figure 1-5c**. Note that these samples did not break during the tests. These results indicate that these monoliths exhibited great mechanical strength. Meanwhile, The values of compressive moduli were obtained by calculation with strains ranging from 0 to 10%. The results are given in **Table 1-2**. It can be observed that the compressive modulus of monoliths increased from 2.24 to 3.46 MPa with increasing POSS amount from 0 to 7.1%. Because POSS reagents with distinctive cage-like structure have good mechanical stability, the mechanical strength of materials can be significantly improved when it is incorporated with the polymer. Water contact angle test was employed to determine hydrophobicity or hydrophilicity of PI and PI-*co*-POSS monoliths. As observed in **Figure 1-6**, the values of the water contact angle of monoliths 8, 11,

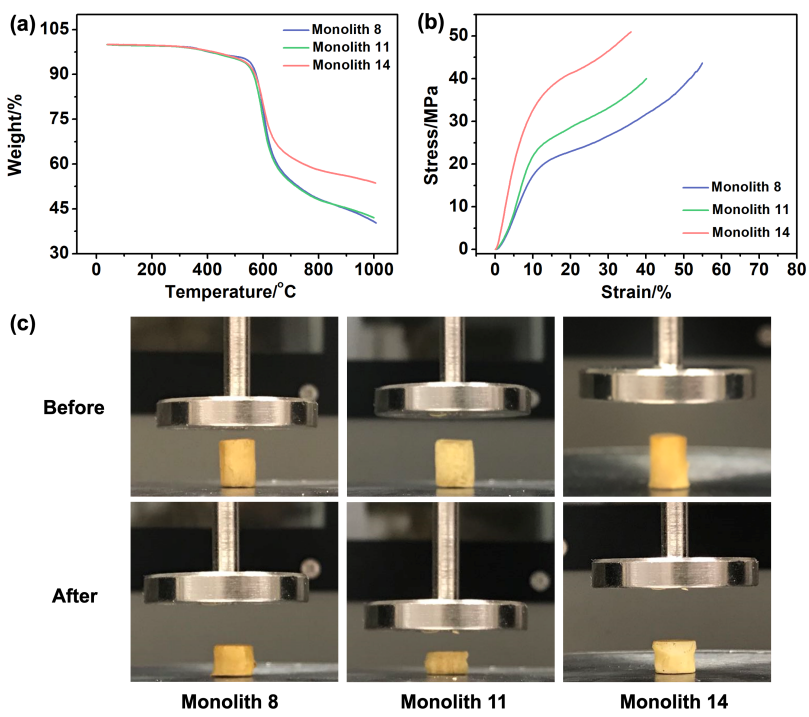

Figure 1-5. (a) TGA curves of monoliths 8, 11, and 14. All the TGA curves were measured at a scanning rate of 10 °C min^{-1} under a nitrogen atmosphere. (b) Mechanical strength test result of compression up to 500 N. (c) Photographs of monoliths 8, 11, and 14 before and after mechanical tests for compression.

and 14 successively increased from 121 to 139 °C with the increasing amount of POSS. Moreover, the comparison of between **Figure 1-6a and Figures 1-6b–c** indicated that the introduction of POSS-epoxy can enhance the hydrophobic property of the monoliths because of the existence of the Si–O–Si structural unit and the $–CH_2–$ hydrophobic groups in POSS-epoxy. These values demonstrate that the skeletons of PI and PI-*co*-POSS monoliths are hydrophobic materials.

Table 1-2. BET surface area and comparison of compressive moduli of PI and PI-*co*-POSS monoliths.

	Monolith 8	Monolith 11	Monolith 14
BET surface area(m^2 g^{-1})	7.05	17.04	17.52
Compressive modulus (MPa)	2.24	2.59	3.46

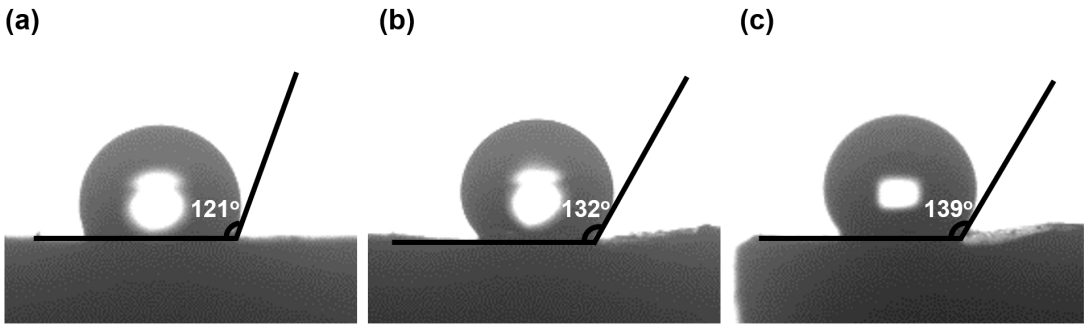

Figure 1-6. Water contact angle of the surface of (a) monolith 8, (b) monolith 11, (c) monolith 14.

1.3.3 Application of PI and PI-*co*-POSS monoliths in oil adsorption

According to the results of the water contact angle test, PI and PI-*co*-POSS monoliths exhibit hydrophobicity. Furthermore, the density of the PI and PI-*co*-POSS monoliths was calculated, and the densities of monoliths 8, 11 and 14 were 0.43, 0.42 and 0.41 g cm^{-3}, respectively. These values were further lower than density of traditional polyimide materials (1.38-1.43 g cm^{-3}), indicating that the resulting PI and PI-*co*-POSS monoliths were rich in macropores and showed higher porosity to facilitate adsorption. Therefore, adsorption tests were employed to investigate the ability of the monoliths to adsorb oil. As shown in **Figure 1-7a**, toluene was dyed with oil red and combined with deionized water. Monolith 14 as example was placed in a bottle containing this mixture of toluene and water. It can be seen that the toluene was instantly and completely adsorbed by the monolith. Similarly, $CHCl_3$ dyed with oil

red was added to deionized water, and this mixture was instantly and completely adsorbed when it contacted with monolith 8, as shown in **Figure 1-7b**. These phenomena demonstrate that the water and oil can be separated by means of the monoliths absorbing oil from the oil–water mixture. Moreover, the oil adsorption capacities of PI and PI-*co*-POSS monoliths were evaluated for various organic solvents and silicone oil. As shown in **Figure 1-7c**, the adsorption capacities for all organic solvents and silicone oil of PI-*co*-POSS monoliths were obviously higher than that for PI monolith. For example, for silicone oil, the adsorption capacities for monoliths 8, 11, and 14 were 1271.4, 2532.7, and 2398.4 mg g^{-1}, respectively. The values for PI-*co*-POSS monoliths were higher than those for similar PI materials [29]. Because the PI-*co*-POSS monoliths exhibited stronger hydrophobicity than PI monolith, as demonstrated by the water contact angle test, it made organic solvents have better wettability on surfaces of the monoliths. Meanwhile, the greater permeabilities and pore size of PI-*co*-POSS monoliths endowed them with high oil adsorption capacities, and their through-pore structure not only provided storage space for organic solvents and oil but also facilitated the mass transfer of substances on the monoliths. We also found that the resulting monoliths swelled during adsorption, the volumes of monoliths 8, 11 and 14 in different solvents were shown in **Table 1-3**. Furthermore, taking chloroform as example, the adsorption capacity of PI and PI-*co*-POSS monoliths could achieve maximum adsorption capacities within 3 min, and did not reduce after 10 cycles (as shown in **Figure 1-8**). It was strongly proved that the resulting materials possessed excellent stability and reusable.

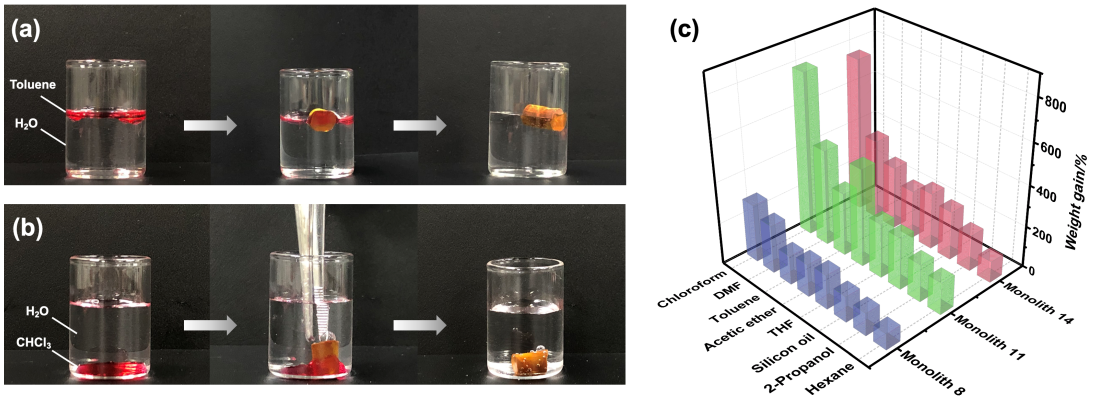

Figure 1-7. Photographs of PI-*co*-POSS monoliths (monolith 14) that adsorbed (a) toluene and (b) chloroform in water. (c) Absorption capacities of monoliths 8, 11, and 14 in organic liquids (tetrahydrofuran,

hexane, DMF, acetic acid, chloroform, toluene, and 2-propanol) and silicone oil.

Table 1-3. The volume of monoliths 8, 11 and 14 in different solvents.

	$V_{Monolith\ 8}$ (mm^3)	$V_{Monolith\ 11}$ (mm^3)	$V_{Monolith\ 14}$ (mm^3)
Dried state	4.4	3.2	3.4
Chloroform	4.6	3.8	4.1
THF	5.3	3.8	4.1
DMF	5.7	4.3	4.6

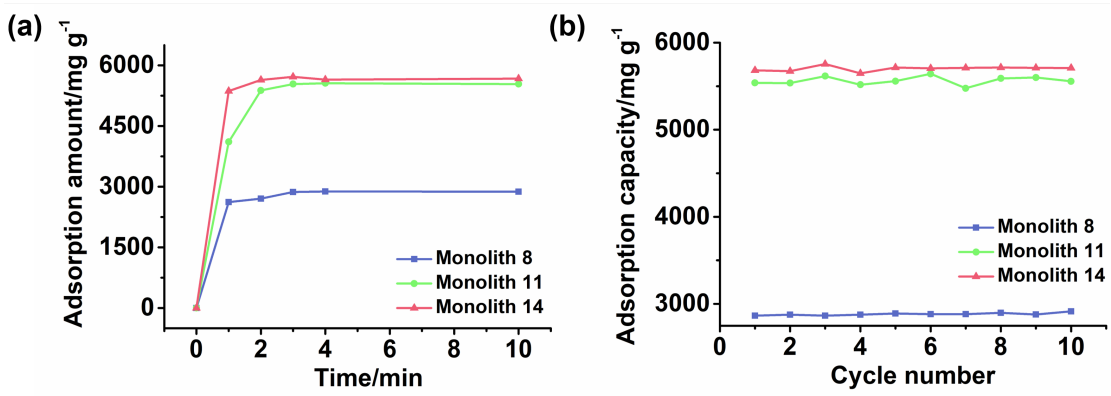

Figure 1-8. (a) The relationship of adsorption time with adsorption amount of chloroform on monolith 8, 11 and 14. (b) Adsorption capacity of chloroform in adsorption-desoprtion cycles on monolith 8, 11 and 14.

In addition, one layer of PI-*co*-POSS monolith could be modified by bPEI which exhibited hydrophilicity. Because of the introduction of POSS-epoxy, some epoxy may be exposed on the skeleton surface of PI-*co*-POSS monolith, indicating that bPEI can modify the PI-*co*-POSS surface. At first, the POSS-epoxy was heated to 300 °C for 20 min and then its ATR-IR spectrum was measured to confirm the stability of the epoxy group after thermal imidization. As observed in **Figure 1-9**, the characteristic peak of the epoxy group in the heated POSS-epoxy appeared at 909 cm^{-1}, demonstrating that most epoxy groups did not decompose but could be modified. In this case, we chose monolith 14 to modify because a greater amount of POSS-epoxy was introduced into the reaction system. The process

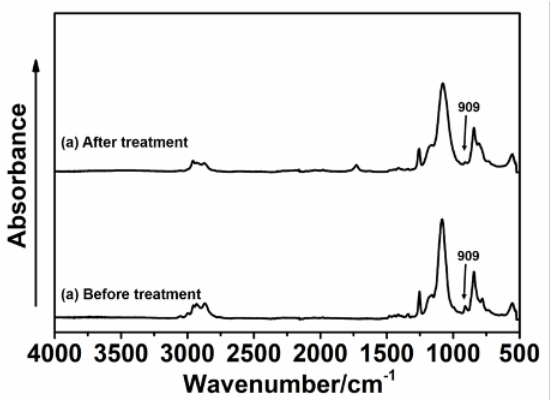

Figure 1-9. ATR-IR spectra of (a) POSS-epoxy heated at 300 °C for 20 min and (b) original POSS-epoxy.

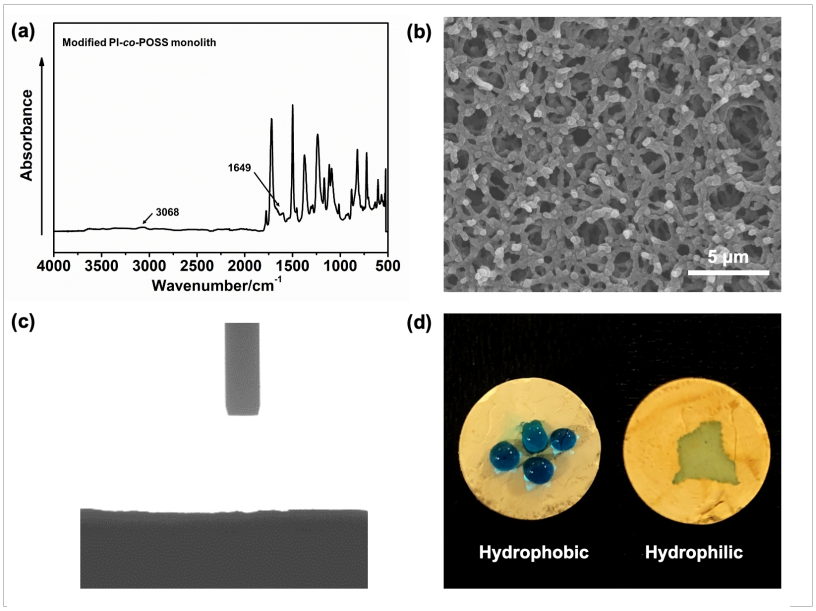

Figure 1-10. (a) ATR-IR spectrum of modified PI-*co*-POSS monolith (modified monolith 14). (b) 2000× magnification SEM image of modified PI-*co*-POSS monolith. (c) Water contact angle of the surface modified PI-*co*-POSS monolith (modified monolith 14). (d) Photographs of water drops on an unmodified layer (hydrophobic) and a modified layer (hydrophilic) of one PI-*co*-POSS monolith.

of modification of PI-*co*-POSS monoliths by bPEI is shown in **Scheme 1-2b**. As observed from the spectrum of modified PI-*co*-POSS monoliths, the peaks at 3068 and 1649 cm^{-1} can be assigned as the characteristic signals of the N–H vibration in primary amine, demonstrating that PI-*co*-POSS monolith was successfully modified (**Figure 1-10a**). And the modified layer in PI-*co*-POSS monolith was characterized by SEM, as shown in **Figure 1-10b**. It can be observed that the homogeneous network structure and through-pore were not damaged after modification. Moreover, the modified PI-*co*-POSS monolith was characterized by TGA, and the result was shown in **Figure 1-11**. There was a slight weight loss before 100 °C, because the modified PI-*co*-POSS monolith is hydrophilic and easy to adsorb water even after dried. When the temperature increased to 200 °C, the modified PI-*co*-POSS monolith appeared notable loss weight because of low thermal stability of bPEI. The result proved that the bPEI was successfully grafted on the PI-*co*-POSS monolith, and decreased thermal stability of the resulting monoliths. Then, water contact angle test was employed to investigate the hydrophilicity of modified layer. As shown in **Figure 1-10c**, water drops can instantly be absorbed on the surface of modified PI-*co*-POSS monolith by bPEI, for which

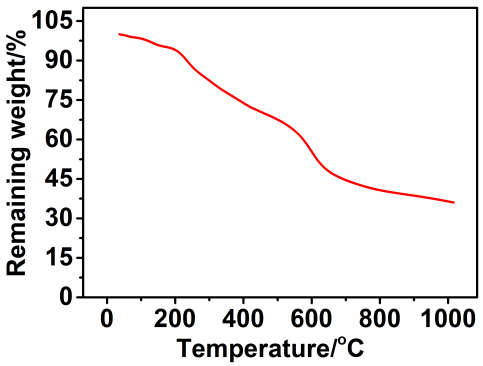

Figure 1-11. TGA curve of modified PI-*co*-POSS monolith (monoliths 14).

the contact angle cannot even be calculated. This phenomenon further demonstrates that the PI-*co*-POSS monolith was successfully modified and exhibited hydrophilicity. Meanwhile, water drops dyed with methyl blue that were dropped on the unmodified layer (hydrophobic layer) cannot be absorbed. However, when the water drops were dropped on the modified layer (hydrophilic layer), they were instantly absorbed (**Figure 1-10d**). These results illustrate that PI-*co*-POSS monoliths have great potential in liquid diode application to achieve oil–water separation because they simultaneously have hydrophilic and hydrophobic layers.

1.4 Conclusions

In this study, a novel, cost-effective, and green synthesis process was developed for the preparations of PI and hybrid PI (PI-*co*-POSS) monoliths with great thermal stability and good mechanical strength, thereby overcoming the existing shortcomings of preparation of PI-based aerogels requiring complicated preparation processes and high cost. In the preparation process, PAA and PAA-*co*-POSS monoliths were first synthesized by TIPS using DMF as good solvent and water as poor solvent. Then PI and PI-*co*-POSS monoliths can be directly obtained by thermal imidization. SEM images and N_2 adsorption–desorption curves of the resulting monoliths demonstrated that they not only had a homogenous pore morphology but also a hierarchical pore structure and through-pore, favouring mass transfer and fluid flow. And the good hydrophobic property of the resulting monoliths was confirmed by water contact angle test. Moreover, through adsorption tests, the resulting monoliths for seven organic solvents and silicone oil were found to exhibit good adsorption performance and can be used in oil–water separation. It would be expected that other PI-based monoliths with great chemical and physical properties can be synthesized *via* this universal approach that can be applied in other fields in the future.

1.5 References

1. C.E. Sroog, Polyimides, *Prog. Polym. Sci.*, 1991, **16**, 561–694.
2. T. Kurosawa, T. Higashihara, M. Ueda, *Polym. Chem.*, 2013, **4**, 16–30.
3. L. Lin, P. Ye, C. Cao, Q. Jin, G.S. Xu, Y.H. Shen, Y.P. Yuan, *J. Mater. Chem. A*, 2015, **3**, 10205–10208.
4. Y. Wang, S. Xu, T. Chen, H. Guo, Q. Liu, B. Ye, Z. Zhang, Z. He, S. Cao, *Polym. Chem.*, 2010, **1**, 1048–1055.
5. Q. Feng, M. Li, T. Wang, Y. Chen, X. Wang, X. Zhang, X. Li, Z. Yang, L. Feng, J. Zheng, H. Xu, T. Zhai, Y. Jiang, *Appl. Catal. B*, 2020, **271**, 118924.
6. J. Liu, J. Tan, Y. Zeng, Y. Liu, K. Zeng, Y. Liu, R. Wu, H. Chen, *Polym. Test.*, 2017, **61**, 83–92.
7. B.S. Ghanem, R. Swaidan, E. Litwiller, I. Pinnau, *Adv. Mater.*, 2014, **26**, 3688–3692.
8. N.C. Pradhan, C.S. Sarkar, S. Niyogi, B. Adhikari, *J. Appl. Polym. Sci.*, 2002, **83**, 822–829.
9. T. Nema, E.C. Chan, P.C. Ho, *J. Pharm. Biomed. Anal.*, 2014, **87**, 130–141.
10. C.M. Parlett, K. Wilson, A.F. Lee, *Chem. Soc. Rev.*, 2013, **42**, 3876–3893.
11. F. Svec, Y. Lv, *Anal. Chem.*, 2015, **87**, 250–273.
12. Y. Zhang, Y. Liu, X. Wang, Z. Sun, J. Ma, T. Wu, F. Xing, J. Gao, *Carbohydr. Polym.*, 2014, **101**, 392–400.
13. S. Mizuno, T.-A. Asoh, Y. Takashima, A. Harada, H. Uyama, *Polym. Degrad. Stab.*, 2019, **160**, 136–141.
14. S. Ungureanu, H. Deleuze, C. Sanchez, M.I. Popa, R. Backov, *Chem. Mater.*, 2008, **20**, 6494–6500.
15. H. Liu, J. Diao, Q. Wang, S. Gu, T. Chen, C. Miao, W. Yang, D. Su, *Chem. Commun.*, 2014, **50**, 7810–7812.
16. Y. Shu, J. Maruyama, S. Iwasaki, Y. Shen, H. Uyama, *Bull. Chem. Soc. Jpn.*, 2017, **90**, 1333–1336.
17. H. Bi, T. Lin, F. Xu, Y. Tang, Z. Liu, F. Huang, *Nano Lett.*, 2016, **16**, 349–354.

18. Y. Wang, S. Ma, L. Zhang, N. Zhang, Y. Li, J. Ou, Y. Shen, M. Ye, *J. Sep. Sci.*, 2019, **42**, 1332–1340.
19. H. Lin, J. Ou, Z. Liu, H. Wang, J. Dong, H. Zou, *Anal. Chem.*, 2015, **87**, 3476–3483.
20. G. Yang, T. Ning, W. Zhao, W. Deng, X. Liu, *RSC Adv.*, 2017, **7**, 16210–16216.
21. J. Lee, J.Y. Chang, *Chem. Commun.*, 2016, **52**, 10419–10422.
22. H. Wang, T. Wang, S. Yang, L. Fan, *Polymer*, 2013, **54**, 6339–6348.
23. Y. Xin, Q. Xiong, Q. Bai, M. Miyamoto, C. Li, Y. Shen, H. Uyama, *Carbohydr. Polym.*, 2017, **157**, 429–437.
24. H. Zhu, Z. Liu, Y. Wang, D. Kong, X. Yua, Z. Xie, *Chem. Mater.*, 2008, **20**, 1134–1139.
25. T. Shimizu, K. Matsuura, H. Furue, K. Matsuzak, *J. Eur. Ceram. Soc.*, 2013, **33**, 3429–3435.
26. X.Y. Yang, L.H. Chen, Y. Li, J.C. Rooke, C. Sanchez, B.L. Su, *Chem. Soc. Rev.*, 2017, **46**, 481–558.
27. J. Kiefer, J.L. Hedrick, J.G. Hilborn, *Adv. Polym. Sci.*, 1999, **147**, 161–247.
28. Y. Lee, J. Huang, S. Kuo, J. Lu, F. Chang, *Polymer*, 2005, **46**, 173–181.
29. J. Kim, J. Kwon, S. Kim, M. Kim, D. Lee, S. Lee, G. Kim, J. Lee, H. Han, *Microporous Mesoporous Mater.*, 2016, **234**, 35–42.
30. Y. Wang, S. Ma, Y. Chen, L. Zhang, J. Ou, Y. Shen, M. Ye, *Talanta*, 2018, **190**, 62–69.

Chapter 2.

Facile preparation of hierarchically porous monolith with optical activity based on helical substituted polyacetylene *via* one-step synthesis for enantioselective crystallization

2.1 Introduction

Helix is an interesting structure universally existed in nature. Before the 20th century, helical structure was limited to use in architecture and aesthetics. Since the discovery of the helix structure of polysaccharide and peptide and the double helix structure of DNA, helical structures have attracted increasing attention by chemists. Subsequently, it was found that helical polymer exhibited many unique properties.[1-4] For example, Green *et al.* discovered that the optical activity of polymers can be amplified by over ten times by utilizing the chiral polymer molecule with helical structure; this phenomenon was termed chiral amplification.[5-6] Owing to these unique properties, helical polymers exhibit great potential in many applications, including chiral catalysis, separation, and sensors.[7-10] In the past few decades, various kinds of helical polymers have been successfully synthesized.[1] Among them, polyacetylene derivatives are considered as a kind of helical polymers with the largest potential in applications, and various materials based on polyacetylene derivatives have been fabricated, such as hybrid nanoparticles, optically active gels, hollow nanoparticles, and porous materials.[11-16]

In recent years, hierarchically porous monolith have attracted considerable attention owing to their various advantageous properties, including high mass transfer efficiency, fast adsorption rate, and easy chemical modification.[17-20] They have been used for various applications, including in separation,[21-23] adsorption,[24] catalysis,[25] and electrochemistry.[26] However, few studies have been conducted on the combination of hierarchically porous monolith and helical polymer with optical activity. At present, only some optically activity porous materials using helical polymer were reported. For example, Deng's group reported that optically active porous materials were fabricated by high internal phase emulsion approach,[27]

and a strategy for establishing chiral three dimensional (3D) porous hybrid foams constructed by optically active helical-substituted polyacetylene and reduced graphene oxide was presented.[28] Although these materials exhibit some good properties, there were still some defects that limited their performances. Because these materials lacked a hierarchically porous structure and exhibits lower specific surface area even in the existence of graphene oxide.

To address the above problems, the author we proposed the preparation of hierarchically porous monolith with optical activity that combined the features of monolith with porous structure and helical polymer with chirality. The present study develops a flexible and highly efficient one-step synthesis of hierarchically porous monolith with good optical activity and large surface area using substituted acetylene and crosslinker in selective porogenic solvent *via* chemically induced phase separation (cross-linking and polymerization induced phase separation). The developed method does not require complicated modification or the use of other supports and allows the achievement of high surface area and hierarchically porous structure with through-pore structure simultaneously, which can provide more chiral sites and space to improve interaction between material and solution. Furthermore, the hierarchically porous monoliths were employed as chiral inducer in enantioselective crystallization.

2.2 Experimental Section

2.2.1 Materials

Isobutyl chloroformate (≥98.0%), (*1S*)-(-)-camphanic acid (≥98.0%), 4-methylmorpholine (≥99.0%), and Boc-D- and Boc-L-alanine were purchased form Tokyo Chemical Industry Co., Ltd. (TCI, Tokyo, Japan). Propargylamine (≥98.0%) and propargyl alcohol, $Rh(nbd)Cl_2$, and sodium tetraphenylboron were purchased from Sigma-Aldrich (St Louis, MO, USA). Concentrated hydrochloric acid (HCl), sodium chloride (NaCl), sodium hydrogen carbonate ($NaHCO_3$), anhydrous magnesium sulfate ($MgSO_4$), benzene, *p*-toluenesulfonic and chloroform ($CHCl_3$) were obtained from Wako Pure Chemical Industries, Ltd. (Wako, Osaka,). Adipic acid (≥99.5%), 2-propanol, tetrahydrofuran (THF), and acetic ether were purchased from Nacalai Tesque, Inc. (Kyoto, Japan). Deionized water was purified by a Milli-Q system (Millipore Inc., Milford, MA).

2.2.2 Synthesis of chiral substituted acetylene and crosslinker

Chiral substituted acetylene (CSA) was synthesize following a previously reported procedure.[29] Briefly, (*1S*)-(-)-camphanic acid (20 mmol) was dissolved in THF (100 mL), and then isobutyl chloroformate (20 mmol) and 4-methylmorpholine (20 mmol) were added into the solution. The solution was stirred for 40 min at 30 °C to sufficiently react. Subsequently, the propargylamine (20 mmol) was slowly dropped into the above solution and was stirred for 4 h at 30 °C. After reaction, the solution was filtered to remove pale-yellow precipitate and the filtrate was collected. The obtained filtrate was dissolved in 100 mL acetic ether and successively rinsed with 2 mol L^{-1} HCl and saturated $NaHCO_3$ aqueous three times. The crude product was dried by anhydrous $MgSO_4$ overnight, and the solvent was removed with vacuum distillation. Finally, crude product was dissolved by THF (2 mL), which was poured into a large amount of hexane for recrystallization to obtain the pure CSA. The crosslinker was synthesized according to a method reported by Nomura et al.[30] Adipic acid (16.9 mmol), propargyl alcohol (59.2 mmol), and *p*-toluenesulfonic acid monohydrate (8.5 mmol) were dissolved in benzene (80 mL), which refluxed for 2 h at 80 °C. The resulting solution was washed by saturated

$NaHCO_3$ and NaCl aqueous solutions. Then, the crosslinker was obtained after reduced pressure distillation. ^{1}H NMR of CSA (400 MHz, $CDCl_3$, δ ppm): 4.6 (d, 2H, −CH≡CC***H***$_2$O−), 2.5 (t, 1H, C***H***≡CCH−), 2.4 (m, 2H, −COC***H***$_2$CH$_2$−), 1.7 (m, 2H, − CH$_2$C***H***$_2$CH$_2$−).

2.2.3 Preparation of the optically active monolith

The [(nbd)Rh$^+$B$^-$(C_6H_5)$_4$][31] as catalyst was weighted in a glass tube, and CSA (58.75 mg) and crosslinker were simultaneously placed into another tube. In a glove box, the mixture of CSA and crosslinker was dissolved using CH_3OH, while the [(nbd)Rh$^+$B$^-$(C_6H_5)$_4$] was dissolved by THF or $CHCl_3$. Then, the two solutions were combined to form a homogeneous prepolymerization solution in a glass tube (6 × 40 mm) purchased from Maruemu Corporation (Osaka, Japan) to prepare monolith. The mixture was placed into a water bath to form optically active monolith. After 8 h, 2-propanol as exchange solvent was employed to replace the previous solvent and remove residue until the washing solution did not show UV signals around 350 nm. Finally, the monolith was dried by vacuum drying for 4 h.

2.2.4 Typical procedure for enantioselective crystallization

The crystallization experiments were performed in a supersaturated solution of racemic Boc-alanine in $CHCl_3$. D- (0.25 g) and L- (0.25 g) Boc-alanine were dissolved in 3 mL $CHCl_3$ and heated to completely dissolve to prepare supersaturated racemic Boc-alanine solution. The prepared monolith was cut into small blocks, and then added into the above supersaturated solution to shake at 35 °C for 1 h. After shaking, in order to form crystals, the mixture was left and slowly cooled to room temperature. The formed crystal was filtered and collected to characterize its optical activity, crystal form, and morphology. The *e.e.* value was calculated as follows: $e.e.\ (\%) = \alpha/\alpha_{max} \times 100\%$, in which α is the optical rotation of a certain mass of formed crystal, α_{max} is the value of optical rotation of commercial enantiopure Boc-L-alanine with same mass as formed crystal.

2.2.5 Instruments and methods

To observe microstructure and pore morphology, the small pieces of the monolithic materials were stuck on the conductive tape to characterize with scanning electron microscopy

(15 kV, SEM, SU-3500 instrument, Hitachi). Attenuated total reflectance infrared (ATR-IR) spectroscopy was performed with a Nicolet iS5 spectrometer (Thermo Scientific, Yokohama, Japan) equipped with an iD5 ATR attachment. The thermogravimetric analysis (TGA) curve was collected with a thermogravimetric analyzer (STA7200RV, Hitachi) by heating from 40 to 800 °C under nitrogen atmosphere. The Brunauer–Emmett Teller (BET) surface area was evaluated by nitrogen adsorption–desorption analysis (Quantachrome Instruments). The pore diameter distribution and pore volume were acquired using density functional theory (DFT) calculations. Circular dichroism (CD) and UV−vis absorption spectra were collected on a spectropolarimeter (J-820 AC, JASCO Corporation, Japan). Optical rotation was determined with a P-2200 polarimeter (JASCO Corporation, Japan). The surface chemistry of the monoliths was determined by X-ray photoelectron spectroscopy (XPS, JEOL JPS-9010MC) with monochromatized Al-Kα radiation (1486.6 eV). Analyzer pass energies was fixed at 60 eV and 10 eV to measure XPS spectra, and binding energies were referred to as C−H (sp3) carbon for the C 1s peak set at 284.6 eV.

According to our previous study,[32] the permeability of the resulting monoliths can be calculated using the equation $B_0 = F\eta L/(\pi r^2 \Delta P)$ (Darcy's law), in which F ($m^3\ s^{-1}$) is the flow rate of the mobile phase, η (Pa s) is the viscosity of the mobile phase (0.89×10^{-3} Pa s for water), L (m) and r (m) are the effective length and inner diameter of the column, respectively, and ΔP (Pa) is the pressure drop across the monolith. To determine the permeability of the obtained monoliths, they were tightly fitted with heat shrink tube and jointed with a digital quantitative tubing pump (As One, DSP-100SA) to control the flow rate of the mobile phase and a digital pressure gauge (Krone, KDM30) to determine pressure drop. Then, the permeability of could be calculated by Darcy's law.

2.3 Results and discussion

2.3.1 Preparation of optically active monolith

In order to obtain a porous structure, thermally induced phase separation (TIPS) was originally adopted to prepare the optically active monolith. CSA was first used to synthesize helical polymer powder to find proper porogenic solvents. However, the selected porogenic solvents, namely CH_3OH, THF, and $CHCl_3$, have low boiling point and are highly volatile at high temperature, which restricts their application in TIPS. Therefore, one-step synthesis was applied in the preparation of porous monolith with optical activity *via* cross-linking and polymerization-induced phase separation. The optically active monolith was prepared according to the process as shown in **Scheme 2-1**.

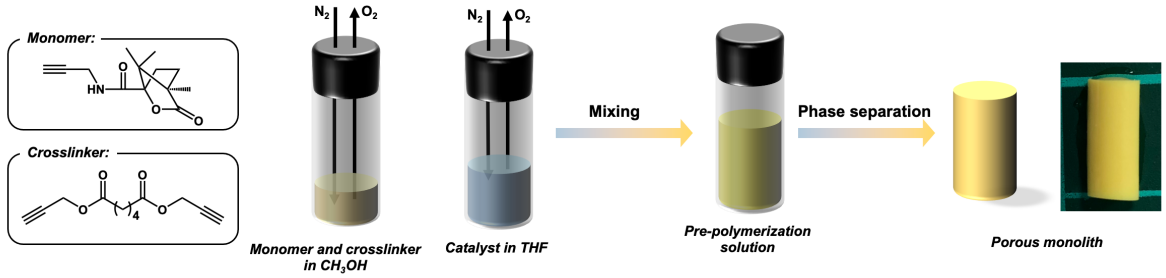

Scheme 2-1. Schematic of the strategy for preparing hierarchically porous monolith with optical activity *via* cross-linking and polymerization-induced phase separation.

To investigate the effects of various factors on the formation of monoliths, the following experimental conditions were optimized: the ratio of the porogenic system, total precursor concentration, the molar ratio of monomer/crosslinker, reaction temperature, and the molar ratio of catalyst/total precursor. The detailed composition of polymerization mixtures, reaction temperature, and the permeability of monoliths are presented in **Table 2-1**. At first, $CHCl_3$ was selected as good solvent considering the solubility of the polymer prepared by CSA, and CH_3OH was chosen as poor solvent. In the porogenic system, the resulting monoliths successfully formed, but their permeability were too low and could not be measured because of extremely large dense structure even in different conditions, such as the ratio of solvent and reaction temperature. This is because the porogenic system restrained domain coarsening of

solute phase during phase separation to generate smaller pore size.[33] The extremely large density is not suitable for practical application. Subsequently, other porogenic system was used to prepare monolith, and THF was chosen as the solvent in porogenic system. As shown in **Table 2-1**, with the decrease of the THF content, the permeabilities of the monoliths 1 and 2 continuously increased from 0.51×10^{-14} m^2 (density: 0.231 g cm^{-3}) to 1.59×10^{-14} m^2 (density: 0.167 g cm^{-3}). This indicated that THF as a good solvent and CH_3OH as a poor solvent could facilitate to form mesopores and macropores, respectively. The result was in accordance with observation by SEM (**Figure 2-1e** and **2-2a** corresponding to monoliths 2 and 1, respectively) that the macropore size increased with the increase in the CH_3OH content. As for monolith 3, the catalyst could not be completely dissolved in CH_3OH to form the homogenous prepolymerization solution. Therefore, the THF/CH_3OH (v/v, 33.3/66.7) was selected as solvent.

Table 2-1. Detailed composition of polymerization mixtures, reaction temperature, and the permeability of monoliths.

Monolith [a]	Monomer/ Crosslinker (n/n)	Total precursor concentration (w/v, %)	Catalyst/ Total precursors (n/n)	THF [b] (wt%)	CH_3OH [b] (wt%)	Temperature (°C)	Permeability ($\times 10^{-14}$ m^2)
1	10/1	15	1/170	46.5	53.5	15	0.51 ± 0.01
2	10/1	15	1/170	33.3	66.7	15	1.59 ± 0.1
3	10/1	15	1/170	23.3	76.7	15	-[c]
4	10/1	10	1/170	33.3	66.7	15	-[d]
5	10/1	20	1/170	33.3	66.7	15	0.25 ± 0.01
6	10/1	15	1/100	33.3	66.7	15	0.15 ± 0.01
7	10/1	15	1/170	33.3	66.7	10	-[c]
8	10/1	15	1/170	33.3	66.7	30	0.09 ± 0.01
9	No crosslinker	15	1/170	33.3	66.7	15	-[d]
10	3/1	15	1/170	33.3	66.7	15	2.04 ± 0.1

[a] Prepolymerization solution contained 58.75 mg monomer.

[b] Weight percentage of solvent in the porogenic system mixture.

[c] Improper proportion of solvents or low temperature led to precipitation of catalyst.

[d] Mechanism strength is too weak, and the prepared monolith easily broke.

Moreover, it is well-known that total precursor concentration has an important influence on the formation of monolithic materials. When the total precursor concentration (crosslinker and CSA) was kept as 10%, the monolith 4 was fragile and its permeability cannot be evaluated owing to the lower density of the skeleton. As the precursor concentration increased from 15% (monolith 2) to 20% (monolith 5), the permeabilities decreased from 1.59×10^{-14} m^2 (density: 0.167 g cm^{-3}) to 0.25×10^{-14} m^2 (density: 0.244 g cm^{-3}). The SEM images could clearly illustrate changes on the macroporous structure of the monoliths 2 (**Figure 2-1e**), 4 (**Figure 2-2b**), and 5 (**Figure 2-2c)**. It could be observed that the macropore size became smaller with the increasing of precursor concentration.

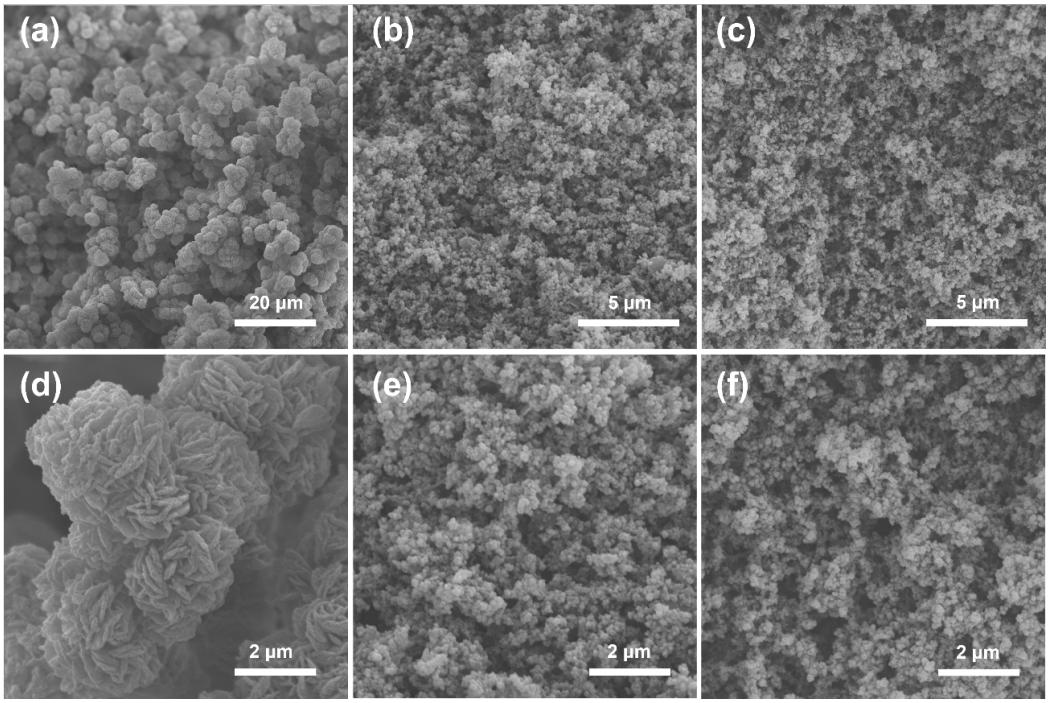

Figure 2-1. Scanning electron microscopy images of (a, d) monolith 9, (b, e) monolith 2 and (c, f) monolith 10. (a) × 1000 magnification, (b, c) × 5000 magnification, (d, e, f) × 10000 magnification.

According to the literature previously reported,[31] $[(nbd)Rh^{+}B^{-}(C_6H_5)_4]$ was selected as catalyst owing to its excellent catalytical performance, because it can contribute to the formation of the helical structure of the polymer through an insert mechanism. In the preparation process of monoliths, different amounts of $[(nbd)Rh^{+}B^{-}(C_6H_5)_4]$ were added into the reaction system to investigate the effects of the molar ratio of catalyst/total precursor for

monoliths. It was obviously found that the permeability of monolith decreased from 1.59 × 10^{-14} m^2 (monolith 2; the molar ratio of catalyst/total precursor: 1/170; density: 0.167 g cm^{-3}) to 0.15 × 10^{-14} m^2 (monolith 6; the molar ratio of catalyst/total precursor: 1/100; density: 0.251 g cm^{-3}) when the molar ratio of catalyst/total precursor increased. As shown in **Figure 2-1e** (monolith 2) and **Figure 2-2d** (monolith 6), it could be seen that the macropore size and permeability decreased as the molar ratio of catalyst/total precursor increased. In addition, the influence of the reaction temperature was also studied. When the reaction temperature was set to 10 ºC (monolith 7), the lower temperature led to the low solubility of catalyst in solvent system which made the catalyst precipitate. This led to the incomplete polymerization between monomer and crosslinker and the formation of a loose matrix. With the increase of the temperature from 15 ºC (monolith 2) to 30 ºC (monolith 8), the prepolymerization solution became homogenous, and the reaction speed was increased resulting a lower permeability (0.09 × 10^{-14} m^2) and larger density (0.253 g cm^{-3}) as shown in **Table 2-1**. Furthermore, as can be clearly observed from **Figure 2-1e** (monolith 2), **2-2e** (monolith 7), and **2-2f** (monolith 8), the macropore size of the monolith decreased as the reaction temperature increased.

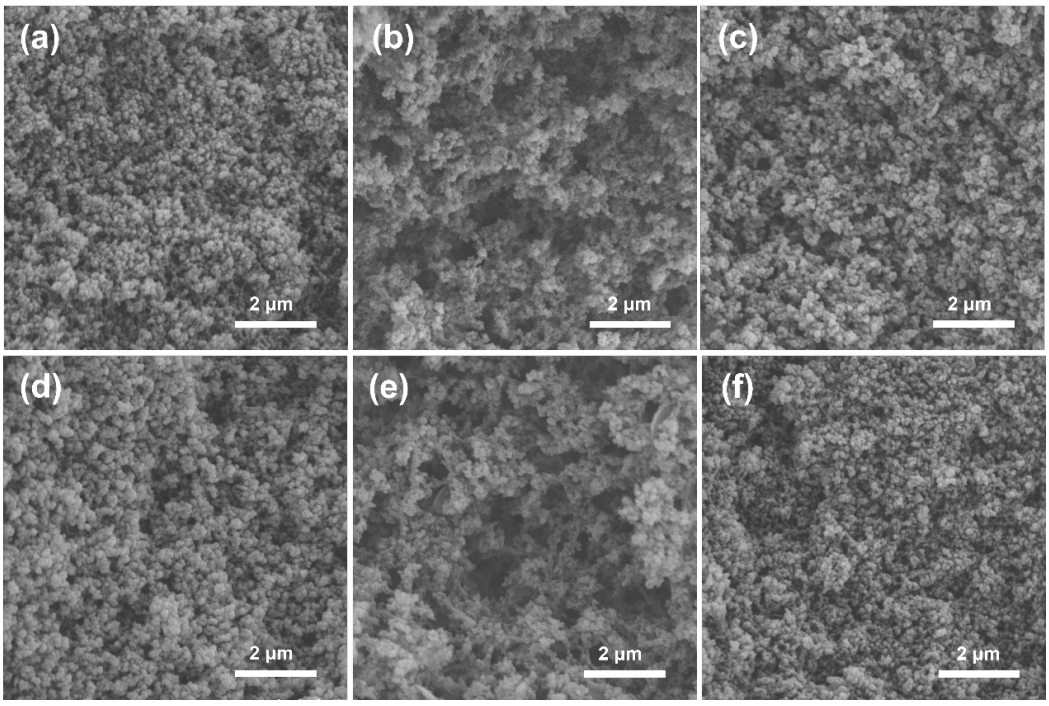

Figure 2-2. SEM images of (a) monolith 1, (b) monolith 4, (c) monolith 5, (d) monolith 6, (e) monolith 7 and (f) monolith 8. (a-f) × 10000 magnification.

The molar ratio of monomer/crosslinker may also affect the formation and permeability of optically active monolith, in addition to its chiral performance. The three monoliths (monoliths 2, 9 and 10) were fabricated with different molar ratio of monomer/crosslinker while keeping the other conditions the same. Monolith 9 without crosslinker was easily broken owing to its low mechanical strength and no cross-linking. After the introduction of the crosslinker, the monoliths showed better mechanical strength and stabler shape. When the molar ratio of monomer/crosslinker increased from 10/1 to 3/1, the permeability increased from 1.59×10^{-14} m^2 (monolith 2, density: 0.167 g cm^{-3}) to 2.04×10^{-14} m^2 (monolith 10, density: 0.145 g cm^{-3}). The addition of crosslinker can improve the mechanical strength of the monolith by improving the degree of crosslinking, and a higher amount of additive can help form a looser skeleton and higher permeability.

The results reported in **Table 2-1** indicated that the permeability and porous structure of the monolith could be adjusted by changing the experimental conditions. In practical application, a suitable pore structure and high permeability of monolith are crucial to achieve good flow-through property. In this study, we finally chose monoliths 2, 9 and 10 prepared with the same molar ratio of catalyst and total monomer (1/170, n/n), and solvent percentage (THF/CH_3OH, v/v, 33.3/66.7) at 15 ^oC to characterize the physical properties and evaluate their performance in application.

2.3.2 Characterization of optically active monolith

In order to prove the occurrence of polymerization and successful preparation of monolithic materials, the monomer (CSA), crosslinker and monoliths 2 and 9 were characterized by ATR-IR spectroscopy (as shown in **Figure 2-3**). The peak signals at 2120 cm^{-1} in the spectra of the monomer and crosslinker (**Figures 2-3a** and **b**) implied the existence of C≡C bonds, while the characteristic peak of C≡C disappeared in monoliths 2 and 9 (**Figures 2-3c and d**). The results indicated that the polymerization successfully proceeded between C≡C bonds in the two monoliths. In addition, the peaks at 3429, 1661 and 1524 cm^{-1} were assigned to amide groups in the monomer. These characteristic peaks of amide groups appeared in

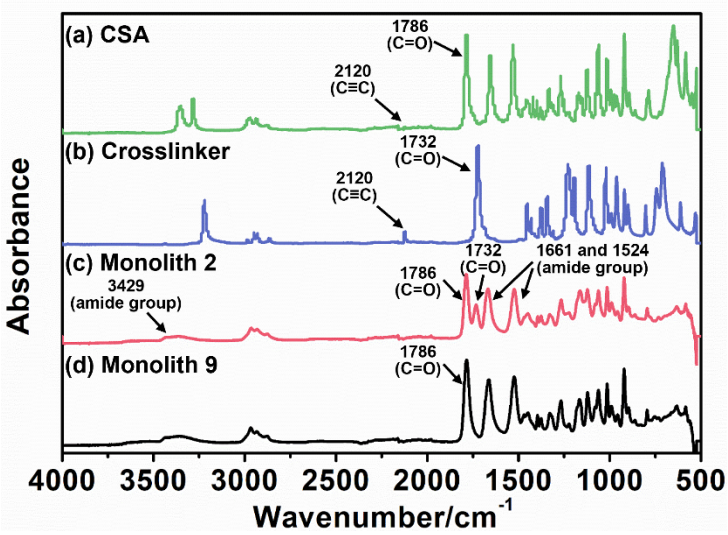

Figure 2-3. Attenuated total reflectance infrared spectroscopy spectra of (a) chiral substituted acetylene (CSA) (monomer), (b) crosslinker, (c) monolith 2, and (d) monolith 9.

spectra of monoliths 2 and 9. A signal of the carbonyl group can be observed at 1786 cm^{-1} in CSA, and it also appeared in the spectrum of monoliths 2 and 9. Compared the spectrums of **Figures 2-3c** and **d**, the signal of the carbonyl group of the easter in the crosslinker at 1732 cm^{-1} did not appeared in monolith 9, nicely indicating that the crosslinker was introduced to reaction system to react with the monomer. The above results clearly demonstrated that the C≡C groups (monomer and crosslinker) were successfully polymerized during the synthesis of the monoliths.

In order to observe the morphology and porous structure, the resulting monoliths with different the molar ratio of monomer/crosslinker were characterized by SEM. The **Figure 2-1** shows the SEM images of monoliths 2, 9 and 10. It can be observed that the monoliths had a uniform 3D pore morphology and contained macropores. Moreover, through-pore existed in monoliths that liquid can pass through the monoliths. It is worth noting that there are many folds on the skeleton surface of monolith 9 in **Figure 2-1d**. And a nitrogen gas adsorption/desorption test was performed to characterize the pore size distribution and specific surface area (as shown in **Figures 2-4a** and **b**). It can be seen from **Figures 2-4a** and **b** that the surface area of monolith 9 is 40.9 m^2 g^{-1}, and the mesopore size is mostly ~4 nm. It indicated that mesopores existed in these folds on the skeleton surface of monolith 9 to increase the surface area and active sites. When the crosslinker was introduced to the reaction system, the monoliths 2 and 10 had large surface area of 69.9 and 51.7 m^2 g^{-1}, respectively. Furthermore, pore size distribution became broader than before the addition of crosslinker. A combination of pore size distribution curves (**Figures 2-4a** and **b**) with SEM images (**Figure 2-1**) reveals that

the monoliths 2 and 10 possessed a hierarchically porous structure. Moreover, they showed higher surface area than the previously reported porous materials constructed by helical polymer with optical activity.[27] The fabricated monoliths possessed a hierarchically porous structure and high surface area that not only provide channels which fluids can pass but also more active sites and space to facilitate interaction between the material and solution.

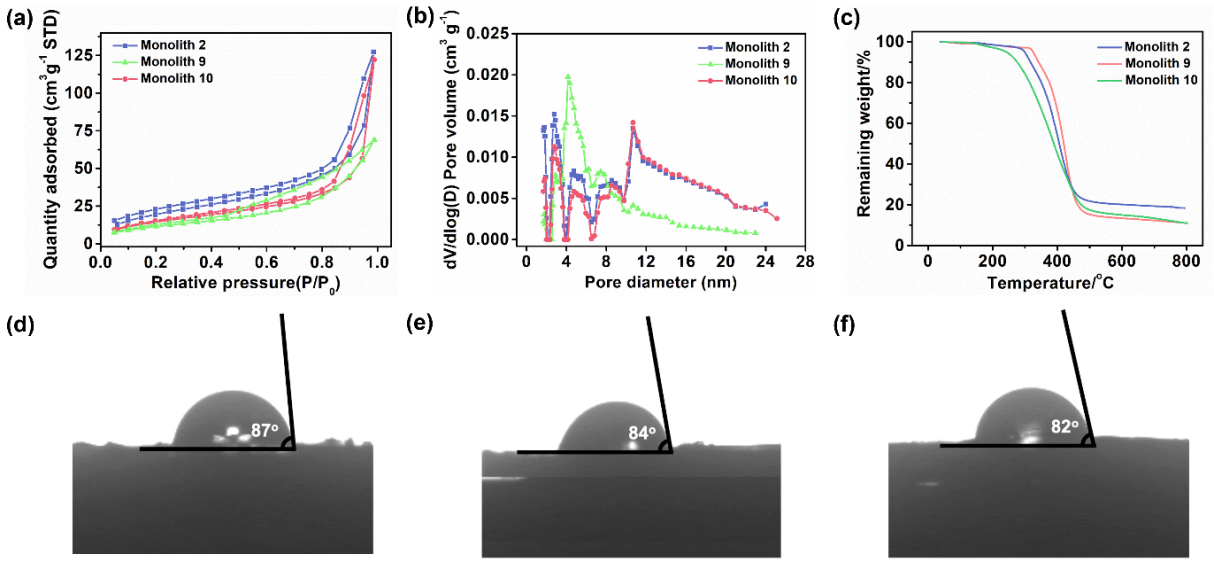

Figure 2-4. (a) Nitrogen adsorption/desorption isotherms of monoliths 2, 9 and 10, and (b) corresponding pore size distribution plots of monoliths 2, 9 and 10. (c) Thermogravimetric analysis (TGA) curves of monoliths 2, 9, and 10. All the TGA curves were measured at a scanning rate of 10 °C min^{-1} under a nitrogen atmosphere. Water contact angle of the surface of (d) monolith 9, (e) monolith 2, and (f) monolith 10.

TGA was employed to study the thermal stability of the three monolithic materials (monoliths 2, 9 and 10). As shown in **Figure 2-4c**, when there is no crosslinker (monolith 9), a significant weight loss occurred as the temperature increased from 320 to 500 °C. When the molar ratio of monomer/crosslinker increased from 10/1 (monoliths 2) to 3/1 (monoliths 10), the starting temperature of the weight loss gradually diminished from 290 to 200 °C. It can be observed that the thermal stability of monoliths reduced after introduction of crosslinker because the crosslinker possessed lower thermal ability and easily decomposed at high temperature as shown in **Figure 2-5**. These results demonstrated that the three monoliths possessed good thermal stability. In addition, to evaluate the hydrophilicity or hydrophobicity, the above monoliths were ground into powder and compressed into smooth tablets to measure

water contact angle. The water contact angles of monoliths 9, 2, and 10 were 87°, 84°, and 82°, respectively (as shown in **Figures 2-4d–f**). It could be observed that their water contact angle reduced in turn with the addition of more crosslinker, and the three monoliths showed extremely weak hydrophilicity. There is a possible reason that more crosslinker with weakly hydrophilic ester group was added into monolith. Furthermore, changes in the thermal stability and water contact angle of the monoliths indicated that the cross-linking agent was successfully introduced into the monolith. In addition, the monoliths 2, 9 and 10 were determined by XPS measurement as shown in **Figure 2-6**. The polymerization occurred in the formation of monoliths is the conversion from C≡C to C=C bond, but the peak of binding energy of C≡C is difficult to be deconvoluted in C 1s high-resolution spectra. Moreover, the atomic percentages were analyzed by low-resolution XPS spectra. As shown in **Table 2-2**, the atomic percentage of N element decreased with the decrease of the molar ratio of monomer/crosslinker. The results indicated that polymerization was successfully occurred in the formation of monolith and the cross-linking agent participated in the reaction.

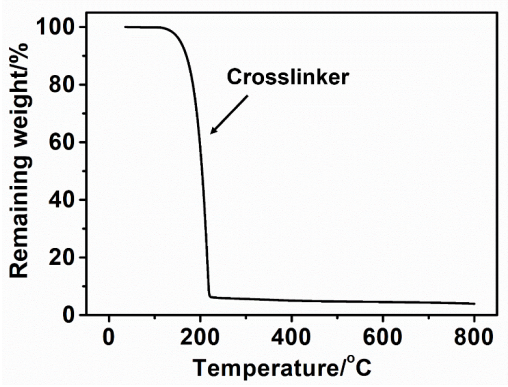

Figure 2-5. TGA curves of crosslinker. The TGA curves were measured at a scanning rate of 10 °C min^{-1} under a nitrogen atmosphere.

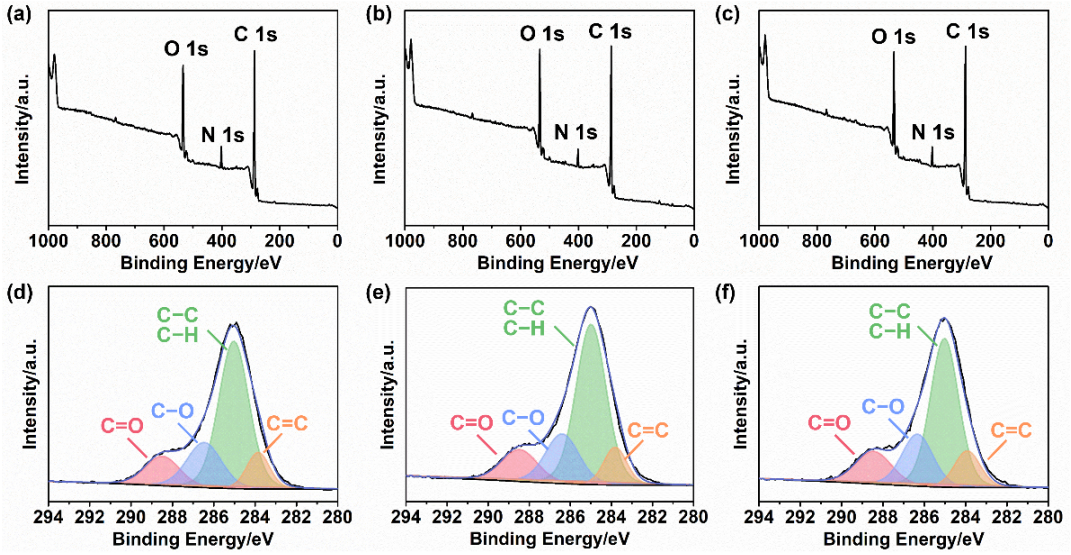

Figure 2-6. Low-resolution XPS spectra of (a) monolith 9, (b) monolith 2 and (c) monolith 10. The C 1s high-resolution spectra of (d) monolith 9, (e) monolith 2 and (f) monolith 10.

Table 2-2. The atomic percentage (%) on the surface of monoliths 2, 9, and 10 detected by XPS spectra.

	C	N	O
Monolith 9	76.77	5.44	17.79
Monolith 2	77.02	4.24	18.74
Monolith 10	74.13	3.87	22.00

The lines were arranged in order of decrease of the molar ratio of monomer/crosslinker.

For practical application, the mechanical properties of monoliths are crucial. In this case, we fabricated cylindrical-shaped monoliths 2 and 10 to measure their mechanical performance by compression experiment in $CHCl_3$ (monolith 9 without crosslinker cannot sustain a good shape and easily broke during exchanging solvent). As shown in the **Figures 2-7a and b**, the two monoliths were subjected to cyclic compressive loading-unloading tests at 40% compressive strain without resting times between two successive measurements. It was found that the curves of five successive loading-unloading cycles of monoliths 2 and 10 almost completely coincided, respectively. As observed in the **Figures 2-7c and d**, the shape and structure of the two monoliths were not destroyed after five compressive loading-unloading tests. These results obviously demonstrated that the two monoliths possessed good fatigue resistance and shape resilience owing to their unique continuous porous structure and high crosslinking degree, which can resist the deformation of shape. These mechanical properties ensured that the fabricated monoliths can be used in relatively severe conditions in practical application.

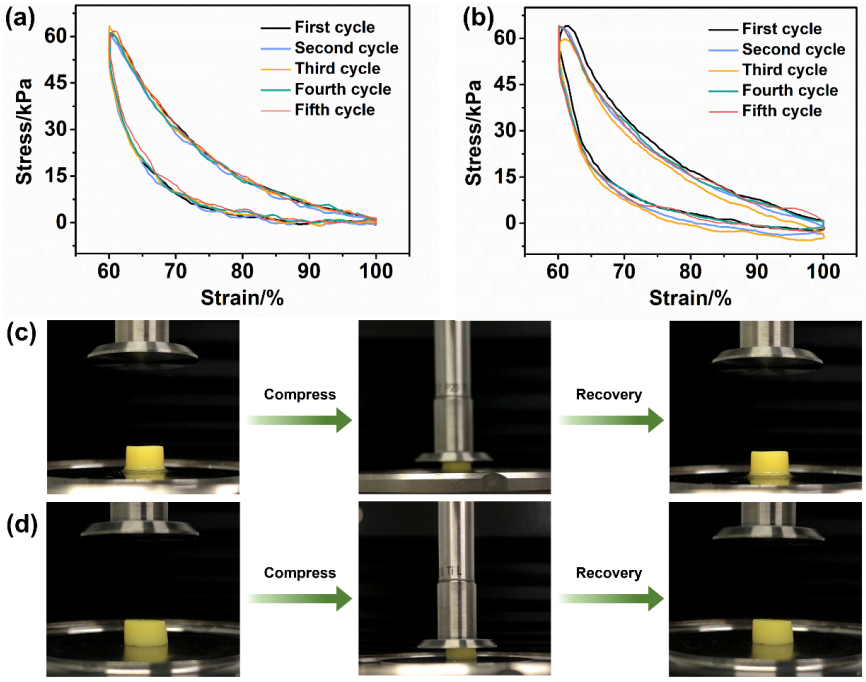

Figure 2-7. Cyclic compressive loading-unloading curves at 40% compressive strain of (a) monolith 2 and (b) monolith 10. Photographs of compression and recovery of (c) monolith 2 and (d) monolith 10.

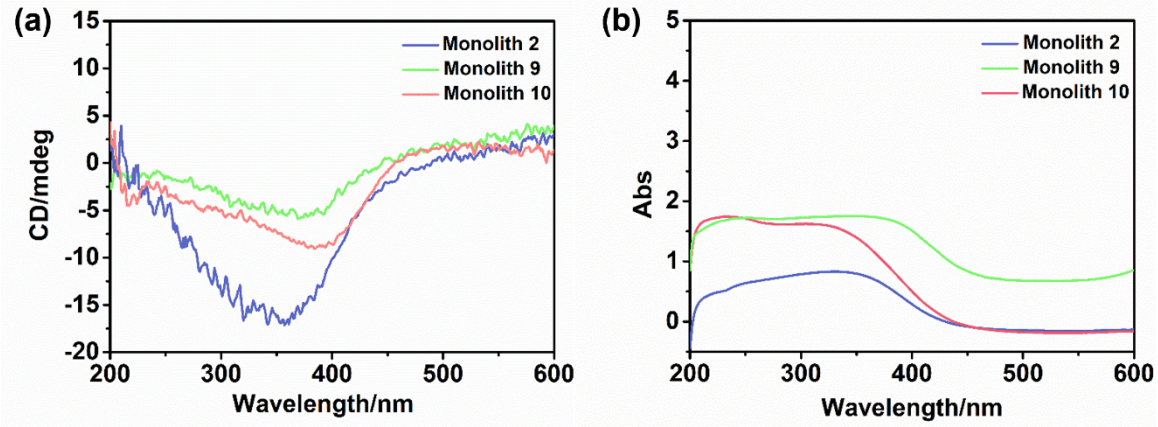

Figure 2-8. (a) Circular dichroism (CD) and (b) UV–vis absorption spectra of monoliths 2, 9 and 10. All spectra were measured by pressed sample with KBr at room temperature.

Substituted polyacetylenes can manifest the helical conformation owing to conjugated structure of the main chain. Generally, the polymers are fabricated by CSA, which can attain a helical conformation with single excess rotation, while the substituted acetylenes without chiral sites exhibit racemic helix conformation with the combination of left-handed and right-handed conformation and the produced polymer cannot manifested optical activity. In order to verify the helical structures and optical activity of the prepared monolith, the CD and UV-Vis spectra were employed to investigate the property (as shown in the **Figure 2-8**). Because the crosslinker was introduced into the monolith with high crosslinking degree, monoliths 2 and 10 cannot dissolved in any solvent to quantitively measure. Therefore, the monoliths 2, 9 and 10 were ground to powder with KBr and compressed to tablets to determine spectra. As shown in **Figure 2-8a**, the negative signals at 375 nm not only appeared in the CD spectra of monolith 9 without crosslinker, as well as in those of monoliths 2 and 10 prepared by copolymer as expected. Simultaneously, the corresponding peaks appeared in the UV-vis adsorption as shown in **Figure 2-8b**. However, the optical activities of the three monoliths cannot be directly compared by the signal intensities of the CD spectrum. Because it is extremely difficult to maintain the same thickness and transparency of the samples that have large influence for the obtained spectra. The solid samples were difficult to quantitively determine. As a result, the resulting monoliths possessed desirable optical activity, and they were constructed by helical conformations with predominantly a one-handed screw sense even in the presence of crosslinker. It indicated that

the monoliths constructed by helical polymer have application potential in several field, such as chiral separation and adsorption.

2.3.3 Application of optically active monolith in enantioselective crystallization

Generally, a pair of enantiomers possessed similar chemical structure and physical properties, but they can achieve completely different functions in the bio-system. Taking thalidomide as example, *R*-thalidomide shows sedative and antiemetic effects on human, while *S*-thalidomide has strong teratogenicity in pregnant woman on embryos.[34] In the late 1950s and early 1960s, pregnant women have been taken racemic thalidomide as medicine for relieving morning sickness, which caused more than 10,000 children in 46 countries were born with deformities. Therefore, the separation of enantiomers is extremely important for humans, indicating that the development of materials used in chiral separation possess great significance.

Enantioselective crystallization as a chiral separation method could be applied to separate racemate. By adding a chiral resolving agent to the saturated solution of the resolved substance, the difference in crystallization rates between the enantiomers of the resolved substance can be induced or expanded to achieve the purpose of chiral resolution.[31, 35] In this case, the resulting monoliths 2 and 10 showed good optical activity, hierarchically porous structure, high surface area, and good mechanical property, and could be used in the enantioselective crystallization. Boc-alanine is used to evaluate the performance of resulting monoliths as chiral source. Subsequently, the two monoliths with optical activity as a chiral resolving agent are respectively added into the saturated solution of the racemic Boc-alanine with shaking for 1 h at 35 ^{o}C. Then, the mixtures are cooled to room temperature for dozens of hours. At the beginning of cooling, Boc-L-alanine possibly preferentially gather on the skeleton surface of monolith to form tiny crystal owing to enantioselective affinity of monolith constructed by helical polymer with optical activity toward Boc-L-alanine molecules (as shown in **Figure 2-9**). It led that the difference in crystallization rate between the Boc-D- and Boc-L-alanine was induced or expanded, then the crystal of Boc-L-alanine preferentially formed. As reference sample, crystallization of racemic Boc-alanine was performed with the same condition in the absence of monoliths. Both crystals obtained in the presence and absence of monoliths were

characterized by SEM. As shown in **Figure 2-10a**, the morphology of the crystal without the addition of monoliths was irregular, and its size was relatively small. As observed in **Figures 2-10b** and **c**, the morphology of the crystals induced by monoliths 2 and 10 had needlelike morphology and were bigger than those obtained without the addition of monoliths. From the SEM images, it can be seen that the two kinds of crystals with addition of monoliths and without addition of monoliths exhibited completely different morphology. To further characterize the crystals induced by monoliths, the CD spectrum was employed to measure the optical activity of induced crystal and residual solution. As observed in **Figures 2-10d** and **e**, the CD spectrum of induced crystal exhibited negative CD signals of which position and direction were uniform with commercial Boc-L-alanine, and the residual solution showed positive CD signals at the same position. These results indicated that Boc-L-alanine was successfully performed enantioselective crystallization from racemic Boc-alanine solution *via* induced by monoliths 2 and 10. The *e.e.* values of induced crystal by monoliths 2 and 10 were 90.3% (α=0.0283, c=1 mg mL^{-1}; yield=58.4%) and 83.9% (α=0.0283, c=1 mg mL^{-1}; yield=59.4%), respectively. This result indirectly demonstrates that the optical activity of monolith 2 was higher than that of monolith 10, indicating that the optical activity is lower with a higher content of crosslinker in monolith. As shown in **Table 2-3**, monolith 2 exhibited better enantioselective ability, higher surface area, and hierarchically porous structure compared to previously reported chiral porous materials. Consequently, the hierarchically porous monolith with optical activity and high

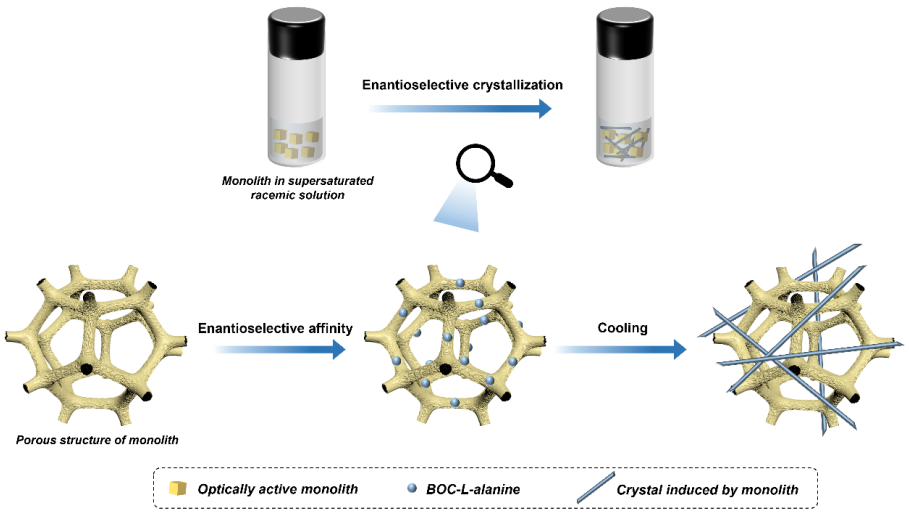

Figure 2-9. Schematic illustration of enantioselective crystallization of Boc-L-alanine using hierarchically porous monolith with optical activity.

surface area constructed by helical substituted polyacetylene exhibited large potential in enantioselective crystallization to purify racemate and obtain enantiopure product.

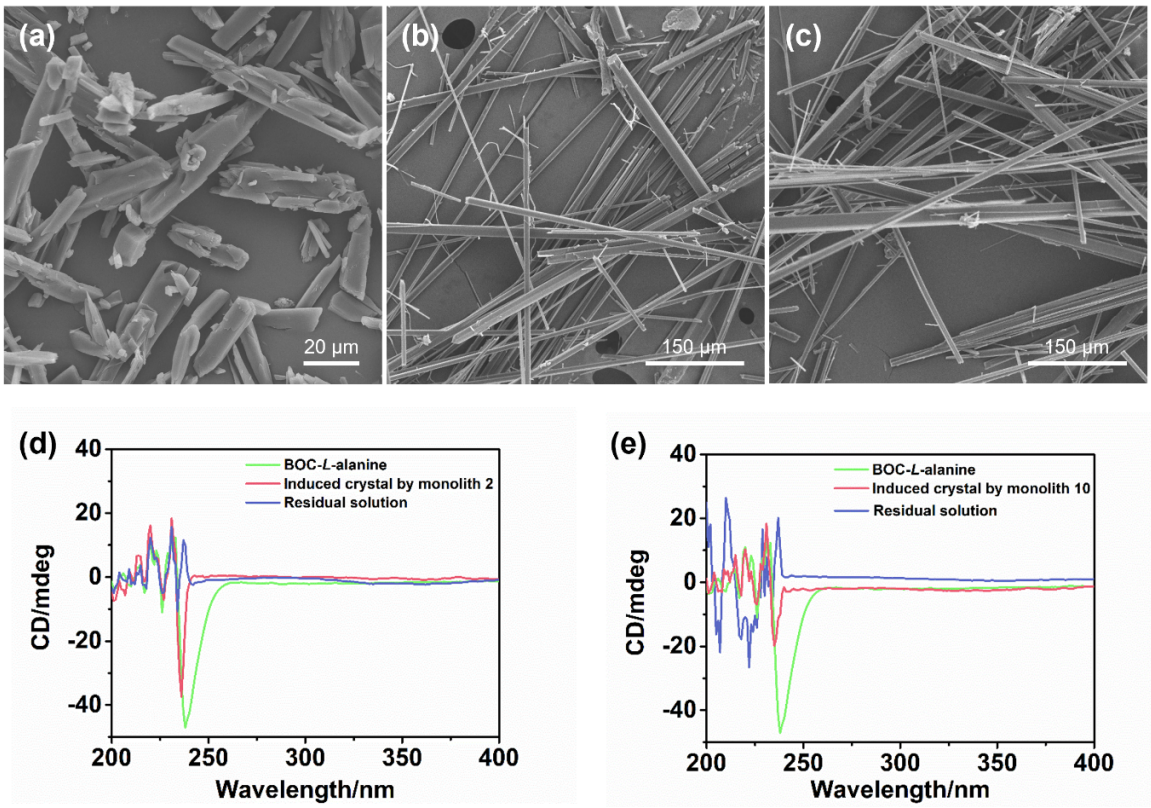

Figure 2-10. SEM images of (a) crystal from racemic Boc-alanine without the addition of monoliths, and crystals induced by (b) monolith 2 and (c) monolith 10 from racemic Boc-alanine. CD spectra of commercial Boc-L-alanine, residual solution, and crystals induced by (d) monolith 2, and (e) monolith 10. All the CD measurements were measured in $CHCl_3$ solution at room temperature.

Table 2-3. Comparison of surface area, performance of enantioselective crystallization, and hierarchically porous structure of different materials.

Material	Surface area (m^2 g^{-1})	*e.e.* (%)	Hierarchically porous structure	Ref.
PolyHIPE-2	15.2	74% (L-threonine)	No	[27]
Foam-2	4.7	88% (L-alanine)	No	[36]
Porous PACA microspheres	Not mentioned	69% (Boc-L-alanine)	No	[37]
Monolith 10	70.0	90%±0.8 (Boc-L-alanine)	Yes	This work

2.4 Conclusions

In this study, hierarchically porous monoliths with optical activity were successfully synthesized by a facile and efficient one-step synthesis. With this method, different porous structure was obtained by setting the appropriate parameters during the cross-linking and polymerization-induced phase separation process. The resulting monolithic materials directly constructed by CSA exhibited good optical activity owing to the orderly helical structure in the main chain. Meanwhile, the SEM images and pore size distribution of the chiral porous monoliths showed hierarchical pore structure and through-pore where the fluid can pass to facilitate sufficient contact between solution and materials. Most importantly, the chiral porous monoliths exhibited higher surface area than other porous monolithic materials with optical activity and without the need for complex doping. The larger surface area and hierarchically porous structure possessed large advantage in application because it leads to more chiral site exposed on the skeleton surface of materials, improving the interaction between the solution and materials. Furthermore, the chiral porous monoliths exhibited good thermal stability and mechanical properties. As a result, the hierarchically porous monoliths with optical activity showed the good performance in enantioselective crystallization. In the future, other porous monoliths with optical activity could be synthesized *via* cross-linking and polymerization-induced phase separation by means of monomers with different functional group to improve their physical and chemical properties and broaden their field of application.

2.5 References

1. E. Yashima, K. Maeda, H. Iida, Y. Furusho, K. Nagai, *Chem. Rev.* 2009, **109**, 6102–6211.
2. J. Shen, Y. Okamoto, *Chem. Rev.* 2016, **116**, 1094–1138.
3. T. Ikai, Y. Okamoto, *Chem. Rev.* 2009, **109**, 6077–6101.
4. T. Nakano, Y. Okamoto, *Chem. Rev.* 2001, **101**, 4013–4038.
5. E. Yashima, K. Maeda, T. Nishimura, *Chem. Eur. J.* 2004, **10**, 42–51.
6. E. Yashima, N. Ousaka, D. Taura, K. Shimomura, T. Ikai, K. Maeda, *Chem. Rev.* 2016, **116**, 13752–13990.
7. L. Yang, Y. Tang, N. Liu, C.-H. Liu, Y. Ding, Z.-Q. Wu, *Macromolecules* 2016, **49**, 7692–7702.
8. H. Hayasaka, T. Miyashita, K. Tamura, K. Akagi, *Adv. Funct. Mater.* 2010, **20**, 1243–1250.
9. Y. Nagata, T. Kuroda, K. Takagi, M. Suginome, *Chem. Sci.* 2014, **5**, 4953–4956.
10. M. Pan, R. Zhao, B. Zhao, J. Deng, *Macromolecules* 2021, **11**, 5043–5052.
11. C. Zhang, L. Liu, Y. Okamoto, *Trends Anal. Chem.* 2020, **123**, 115762.
12. K. Maeda, E. Yashima, *Top. Curr. Chem.* 2017, **375**, 1–33.
13. G. Shi, X. Dai, Y. Zhou, J. Zhang, J. Shen, X. Wan, *Polym. Chem.* 2020, **11**, 3179–3187.
14. B. Zhao, X. Gao, N. Lu, J. Deng, *Adv. Opt. Mater.* 2020, **8**, 2000858.
15. P. Li, J. Feng, K. Pan, J. Deng. *Macromolecules* 2020, **53**, 602–608.
16. J. Z. Sun, A. Qin, B. Z. Tang, *Polym. Chem.* 2013, **4**, 211–223.
17. M. V. Santos, É. Pecoraro, S. H. Santagneli, A. L. Moura, M. Cavicchioli, V. Jerez, L. A. Rocha, L. F. C. de Oliveira, A. S. L. Gomes, C. B. de Araújo, S. J. L. Ribeiro, *J. Mater. Chem. C* 2018, **6**, 2712–2723.
18. M. Hartmann, W. Schwieger, *Chem. Soc. Rev.* 2016, **45**, 3311–3312.
19. H. Zhang, X. Li, Y. Yao, S. Ma, Z. Liu, J. Ou, Y. Wei, M. Ye, *Anal. Chim. Acta* 2019, **1046**, 199–207.
20. A. Feinle, M. S. Elsaesser, N. Husing, *Chem. Soc. Rev.* 2016, **45**, 3377–3399.
21. Y. Okamoto, K. Suzuki, K. Ohta, K. Hatada, H. Yuki, *J. Am. Chem. Soc.* 1979, **101**, 4763–

4765.

22. G. Hasegawa, K. Morisato, K. Kanamori, K. Nakanishi, *J. Sep. Sci.* 2011, **34**, 3004–3010.
23. I. Nischang, T. J. Causon, *Trends Anal. Chem.* 2016, **75**, 108–117.
24. X. Ge, Y. Ma, X. Song, G. Wang, H. Zhang, Y. Zhang, H. Zhao, *ACS Appl. Mater. Interfaces* 2017, **9**, 13480–13490.
25. Z. T. Xie, T. A. Asoh, H. Uyama, *Carbohydr. Polym.* 2019, **214**, 195–203.
26. G. Hasegawa, K. Kanamori, T. Kiyomura, H. Kurata, T. Abe, K. Nakanishi, *Chem. Mater.* 2016, **28**, 3944–3950.
27. J. Liang, Y. Wu, X. Deng, J. Deng, *ACS Macro Letters* 2015, **4**, 1179–1183.
28. W. Li, B. Wang, W. Yang, J. Deng, *Macromol. Rapid Commun.* 2015, **36**, 319–326.
29. K. Zhou, L. Tong, J. Deng, W. Yang, *J. Mater. Chem.* 2010, **20**, 781–789.
30. R. Nomura, K. Yamada, J. Tabei, Y. Takakura, T. Takigawa, Masuda. T, *Macromolecules* 2003, **36**, 6939–6941.
31. B. Chen, J. Deng, W. Yang, *Adv. Funct. Mater.* 2011, **21**, 2345–2350.
32. Y. Wang, L. Zhang, T. Asoh, H. Uyama, *Mater. Adv.* 2021, **2**, 3560–3568.
33. K. Nakanishi, S. Naohiro, *J. Am. Ceram. Soc.* 1991, **74**, 2518–2530.
34. K. B. E. Fischer, N. Thoma, *Nature* 2014, **512**, 49–53.
35. Y. Mastai, *Chem. Soc. Rev.* 2009, **38**, 772–780.
36. B. Wang, W. Li, J. Deng, *J. Mater. Sci.* 2017, **52**, 4575–4586.
37. C. Chen, B. Zhao, J. Deng, *ACS Macro Lett.* 2015, **4**, 348–352.

Chapter 3.

Facile fabrication of hierarchically porous boronic acid group-functionalized monoliths with optical activity for recognizing glucose with different conformation

3.1 Introduction

Phenylboronic acid (PBA) is a unique molecule that can specifically recognize compounds containing *cis*-diol groups, such as catechol, polysaccharides, and glycoproteins, *via* reversible covalent bonds with great research significance in the fields of environmental, food, and biological detection.[1-6] Under high-pH conditions, PBA can form covalent bonds with the *cis*-diol group-containing compounds, which dissociate under low pH yielding pristine PBA and the *cis*-diol group-containing compounds. Thus, PBA and its derivatives exhibit a broad range of application prospects in biosensors, drug delivery and release, enrichment, and imaging.

It is well known that macromolecules in organisms often have chirality, which is closely related to the normal life activities of the organisms.[7] It has been suggested that developing chiral materials is of great significance to human life.[8] For instance, drugs with chirality are frequently applied in clinical treatments. Further, chiral substances are ubiquitous in nature, including in amino acids, polysaccharides, and proteins.[9] For example, almost all natural amino acids that constitute proteins are in the L-conformation, while almost all natural monosaccharides are in the D-conformation. Chiral compounds with the same conformation often tend to interact with each other. In most cases, a pair of enantiomers significantly differs in its pharmacological activity, metabolism, and toxicity in vivo;[10] thus, developing techniques to obtain a single enantiomer is critical for pharmaceutical applications. However, the pair is very similar in its physical and chemical properties, making it difficult to separate the individual enantiomers. Although it is evident that incorporating a PBA functional group and chirality is meaningful, there is limited research in this area.

Recently, a series of helical polymers with desirable optical activity was synthesized. Helical polymers have attracted much attention because of their unique chiral amplification

derived from the high tacticity of the main chain.[11-15] Thus, they have exhibited great potential in many fields, such as molecular recognition, asymmetric catalysis, and chiral separation. Currently, most of the materials based on helical polymers are nanoparticles[16-18] or microspheres,[19-22] which are inconvenient for practical applications. Therefore, developing monolithic materials based on helical polymers is necessary.

A hierarchically porous monolith as a novel material simultaneously contains two or more pore scales, including micropores (<2 nm), mesopores (2–50 nm), and macropores (>50 nm).[23] The presence of micropores and mesopores can provide a more active center and larger surface area, while macropores can accelerate mass transfer. These materials have several advantages, such as ease of use, a porous structure, faster mass transfer rate, and good stability. They have been widely used in applications such as separation, exploitation of energy resources, and catalysis.[24-28] Previously, we fabricated a hierarchically porous monolith with optical activity using crosslinking and polymerization-induced phase separation (CPIPS), which performed well in enantioselective crystallization.

In this study, we synthesized hierarchically porous boronic acid group-functionalized monoliths with optical activity using chiral and achiral substituted acetylenes as monomers to further develop the preparation method and introduce a functional group. Multiple characterizations were adopted to obtain the physical and chemical property of the monoliths. The synthesized monoliths have the potential in recognition, separation, and adsorption of substances with chirality and *cis*-diol groups.

3.2 Experimental Section

3.2.1 Materials

Isobutyl chloroformate (≥98.0%), 4-carboxyphenylboronic acid (≥97.0%), 4-methylmorpholine (≥99.0%), (*R*)-(-)-2-phenylpropionic acid (≥98.0%), and (*S*)-(+)-2-phenylpropionic acid (≥98.0%) were purchased from Tokyo Chemical Industry Co., Ltd. (TCI, Tokyo, Japan). Bicyclo[2.2.1]hepta-2,5-diene-rhodium(I) chloride dimer ($Rh(nbd)Cl_2$, ≥96%), propargylamine (≥98.0%), propargyl alcohol, and sodium tetraphenylboron were obtained from Sigma–Aldrich (St Louis, MO, USA). α-D- and α-L-Glucose were purchased from Thermo Fisher Scientific (Geel, Belgium). Anhydrous magnesium sulfate ($MgSO_4$), benzene, sodium chloride (NaCl), sodium hydrogen carbonate ($NaHCO_3$), 2 mol L^{-1} hydrochloric acid (HCl), *p*-toluenesulfonic acid monohydrate, super dehydrated tetrahydrofuran (THF), super dehydrated methanol (CH_3OH), chloroform ($CHCl_3$), and potassium bromide (KBr, infrared (IR) grade) were purchased from Wako Pure Chemical Industries, Ltd. (Wako, Osaka, Japan). Adipic acid (≥99.5%) and other solvents (tetrahydrofuran, 2-propanol, acetic ether, and ethanol) were acquired from Nacalai Tesque, Inc. (Kyoto, Japan).

3.2.2 Synthesis of chiral and achiral substituted acetylene

Chiral substituted acetylene (*R*-monomer 1, *R*-M1; *S*-monomer 1, *S*-M1) and achiral substituted acetylene (monomer 2, M2) were synthesized according to a previously reported method.[29, 30] The chiral substituted acetylene was synthesized as follows: Briefly, *R*-M1 or *S*-M1 (10 mmol, 1.5 g) were dissolved in THF, followed by slowly dropping isobutyl chloroformate (10 mmol, 1.36 g) and 4-methylmorpholine (10 mmol, 1.01g) in sequence. The mixture was reacted at 30 °C while stirring for 40 min, after which propargylamine (10 mmol, 0.51 g) was added dropwise into the solution and stirred for 4 h at 30 °C. Subsequently, the pale-yellow precipitate was removed by filtration to obtain the crude product, which was dissolved in acetic ether (100 mL). Then, 2 mol L^{-1} HCl (30 mL) and saturated $NaHCO_3$ aqueous (30 mL) were used to wash the obtained solution three times, respectively. After drying the obtained product over anhydrous $MgSO_4$ for 12 h, it was vacuum distilled to remove any

solvent. Finally, the crude product was dissolved in THF (4 mL), which was dropped into a large amount of hexane for recrystallization to acquire the pure chiral substituted acetylene (*R*-M1 or *S*-M1). ^{1}H NMR of R-M1 or *S*-M1 (400 MHz, $CDCl_3$, δ ppm): 5.4 (s, 1H, −CH_2N***H***CO−), 4.0 (m, 2H, CH≡CC***H***$_2$NH−), 3.5 (m, 1H, −COC***H***CH_3Ph), 2.2 (t, 1H, C***H***≡CCH−), 1.5 (t, 3H, −C***H***$_3$). The synthesis process of the achiral substituted acetylene (M2) is similar to that of chiral substituted acetylene with some modifications. 4-carboxyphenylboronic acid (10 mmol, 1.7 g) was selected as the precursor for the achiral substituted acetylene, while the other steps remained the same. ^{1}H NMR of M2 (400 MHz, $CDCl_3$, δ ppm): 8.9 (t, 1H, −CH_2N***H***CO−), 8.1 (s, 2H, B(O***H***)$_2$−), 4.0 (m, 2H, ≡CHC***H***$_2$NH−), 3.1 (t, 1H, C***H***≡CCH−).

3.2.3 Preparation of the monolithic materials

First, adipic acid and propargyl alcohol were used as precursors to synthesize the crosslinker according to a previously reported method.[31] [(nbd)$Rh^+B^-(C_6H_5)_4$] was used as the catalyst, which was prepared using Rh(nbd)Cl_2 and sodium tetraphenylboron.[32] Then, the crosslinker (5.6 mg) and monomers (M1: 32.8 mg, M2: 15.2 mg) were weighed in tube A, and the catalyst (0.9 mg) in tube B. The two tubes were flushed with nitrogen to ensure an inert atmosphere and placed into a glove box. Then, super dehydrated CH_3OH (232 μL) was added to tube A to dissolve the monomers and crosslinker, and super dehydrated THF (36 μL) was added to tube B to dissolve the catalyst. The two solutions were sufficiently mixed with each other and placed in a water bath at 15 °C for 8 h. The obtained monolith was sufficiently washed with 2-propanol, ethanol, and deionized water in sequence to replace the previous solvents and remove any residue, followed by vacuum drying for 8 h.

3.2.4 Selectively chiral adsorption test

First, the 0.5 mg mL^{-1} α-D- and α-L-glucose were prepared using phosphate buffer (PB) solution (pH=8.6) as solvent, and the monoliths to be tested were cut into slices. Subsequently, 30 mg monolith were added into 2 mL 0.5 mg mL^{-1} α-D- or α-L-glucose to shake for 12 h at 10 °C without light. After adsorption, the monoliths were washed by 1% triethylamine (TEA)

aqueous solution for three times to remove unabsorbed α-glucose and salt in PB solution, followed by vacuum drying for 8 h to test water contact angle.

3.2.5 Characterization

Attenuated total reflectance IR (ATR-IR) spectra were obtained using Nicolet iS5 spectrometer outfitted with an iD5 ATR attachment (Thermo Scientific, Yokohama, Japan). The pore morphology of the hierarchically porous monolithic material was observed using scanning electron microscopy (SEM, 15 kV, SU-3500 instrument, Hitachi, Japan). The nitrogen adsorption/desorption isotherms were obtained using a surface area and pore size analyzer (NOVA 4200e, Quantachrome Instruments, USA). Density functional theory (DFT) was used to calculate the pore size distribution and pore volume. A thermogravimetric analyzer (STA7200RV, Hitachi, Japan) was employed to record the thermogravimetric analysis (TGA) curves by heating from 40 to 800 °C under nitrogen atmosphere with a scanning rate of 10 °C min^{-1}. The Raman spectra were collected by a Raman spectrometer (NRS-3100, JASCO Corporation, Japan) with a 532 nm laser as an excitation source under 100 mW power. Circular dichroism (CD) spectroscopy and ultraviolet–visible (UV−vis) absorption spectrometry were performed using a spectropolarimeter (J-820 AC, JASCO Corporation, Japan). To determine the surface chemistry of the hierarchically porous monolith, the X-ray photoelectron spectroscopy (XPS, JEOL JPS-9010MC) was employed to characterize them with monochromatized Al-Kα radiation (1486.6 eV). The analyzer pass energies were fixed at 30 eV for wide XPS spectra and 50 eV for narrow XPS spectra. The binding energies were referred to as C−H (sp3) carbon for the C 1s peak set at 284.6 eV. The contact angle was determined using a Drop Master DM300 (Kyowa Interface Science, Japan) with 1.0 μL solution drops.

To measure the permeability, the obtained cylindrically-shaped monolith was tightly fitted with a proper heat shrink tube and connected to a digital pressure gauge (Krone, KDM30, Japan) to obtain ΔP, while a digital quantitative tubing pump (As One, DSP-100SA, Japan) was used to control the flow rate of the mobile phase.

3.3 Results and discussion

3.3.1 Preparation of the hierarchically porous boronic acid group-functionalized monolith with optical activity

In our previous study, we developed a flexible and highly efficient "one-step" method, the CPIPS method, to prepare chiral hierarchically porous monoliths.[33] To further develop this "one step" method and broaden its feasibility, we attempted to fabricate functionalized porous monoliths with optical activity using M1 with a chiral center, M2 with a boronic group, and a crosslinker as the raw materials. The helical polymer with chirality and the boronic acid functional group can interact with chiral and *cis*-diol group-containing compounds.[30] The detailed preparation procedure is shown in **Scheme 3-1**.

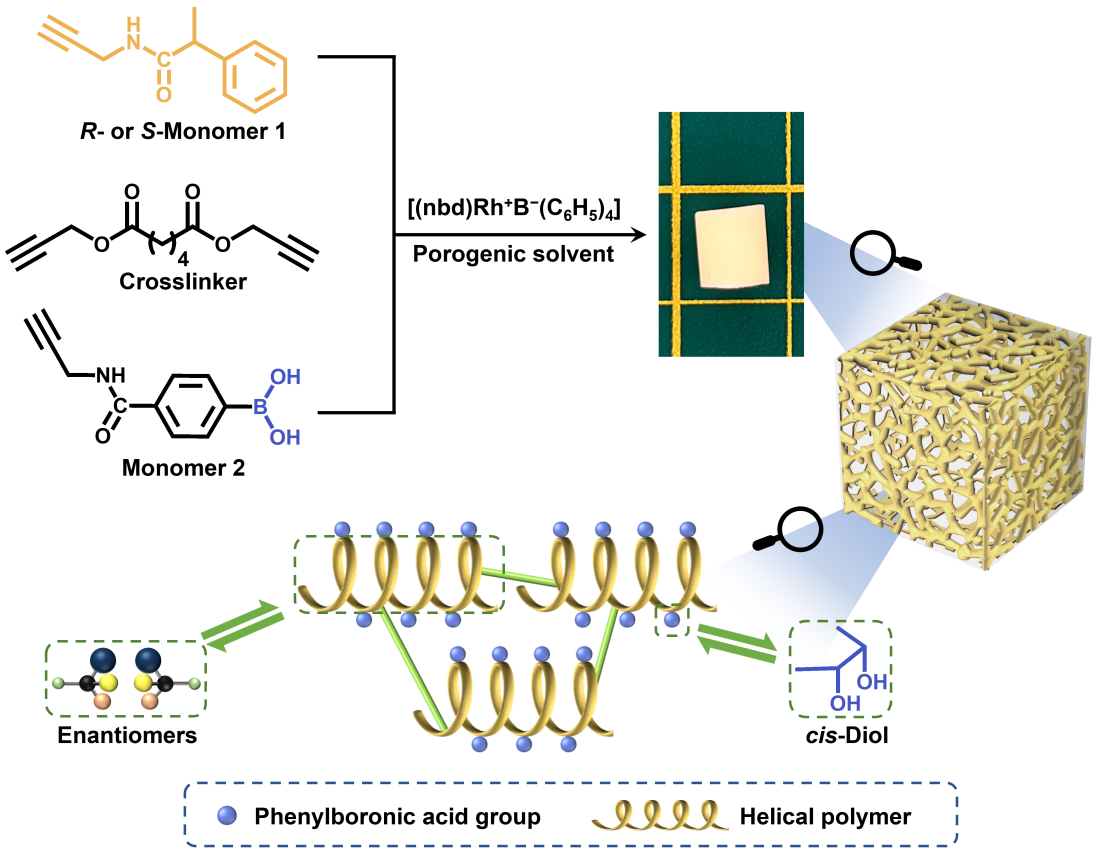

Scheme 3-1. Strategy for preparing the hierarchically porous boronic acid group-functionalized monolith with optical activity *via* crosslinking and polymerization-induced phase separation.

For the preparation of porous monolith, the composition of the pre-polymerization solution and the proportion of porogenic solvent have a significant influence on its morphology; therefore, the preparation conditions were optimized as shown in **Table 3-1**. It has been suggested that the porogenic solvent plays a particularly important role in the formation of the monolith. Therefore, preliminary trials using different porogenic solvents, such as THF/polyethylene glycol (PEG) 200, THF/1-propanol, and THF/CH_3OH, were conducted. When any proportion of THF/1-propanol or THF/PEG200 was used as porogenic system, the monolith cannot be formed, or there is no pore structure in monolith. Considering their porogenic ability and dissolving capacity, binary THF/CH_3OH was eventually selected as the porogenic solvent for this study. The molar ratio of *R*-M1 and M2 was maintained at 3/1 to investigate the effect of the amount of THF/CH_3OH on the monolith. As observed in **Table 3-1**, at 29.9% THF, the permeability of monolith II was 0.16×10^{-14} m^2, which increased to 2.58×10^{-14} m^2 at 13.4% THF for monolith III**.** Furthermore, SEM images of monolith II and III (**Figure 3-1a, b, e, and f**) indicate that a lower content of CH_3OH in the porogenic solvent yielded fewer large macropores. These results suggest that THF as the microporogenic solvent facilitates the formation of micropores and mesopores, while CH_3OH is the macroporogenic component in the porogenic system.

It was also observed that the concentration of the total precursors influenced the porous morphology and permeability of the monolith (**Table 3-1)**. The permeability decreased from 2.58×10^{-14} m^2 (monolith III) to 0.25×10^{-14} m^2 (monolith IV) with an increase in the total precursor concentration. The SEM images of the two monoliths (**Figure 3-1b, c, f, and g**) also confirmed the emergence of the larger macropores with the decrease of the total precursor concentration. As a result, a monolith with good permeability and more macropores could be fabricated in the presence of THF/CH_3OH (v/v, 13.4/86.6) as the porogenic solvent and 20% total precursors concentration in the pre-polymerization solution. Hence, the permeability and macropore size of the prepared monolith could be adjusted by changing the composition of the pre-polymerization solution. Therefore, under the same conditions, monolith V was prepared using *S*-M1 as the monomer, yielding a good permeability of 2.52×10^{-14} m^2, which was almost

equal to that of monolith III. The same conditions were also employed to fabricate monolith I without M2 and monolith VI without M1. However, monolith I was fragile and fractured, while monolith VI was transparent without a porous structure; therefore, their permeability could not be measured. Because the raw materials in prepolymerization solution were changed, the optimized preparation conditions may not have been suitable for fabricating monoliths I and VI. To further investigate these differences, monoliths I, III, V, and VI were selected for subsequent characterization.

Table 3-1. Composition of the polymerization mixtures and the permeability of the monoliths.

Monolith [a]	[*R*-M1]/[*S*-M1]/[M2] (mol/mol/mol)	THF [b] (wt%)	CH_3OH [b] (wt%)	Total precursors concentration (w/v, %)	Permeability ($\times 10^{-14}$ m^2)
I	4/0/0	13.4	86.6	20	-[c]
II	3/0/1	29.9	70.1	20	0.16
III	3/0/1	13.4	86.6	20	2.58
IV	3/0/1	13.4	86.6	30	0.25
V	0/3/1	13.4	86.6	20	2.52
VI	0/0/4	13.4	86.6	20	-[d]

[a] The molar ratio of the total monomers/crosslinker in the pre-polymerization solution was maintained at 10/1, the molar ratio of total precursors/catalyst was kept at 157/1, and the reaction temperature was set to 15 °C for 8 h.

[b] Weight percentage of the solvent in the porogenic mixture system.

[c] The monoliths easily fractured during measurement.

[d] The pressure drop was too high to measure permeability.

3.3.2 Characterization of the hierarchically porous boronic acid group-functionalized monolith with optical activity

Hierarchically porous materials combine the merits of micropores, mesopores, and macropores, thereby showing large potential in many fields.[34, 35] To confirm the hierarchically porous structures, the micro morphology of monoliths III and V was observed using SEM. Monoliths III and V showed a homogeneous and uniform porous structure, with macropores of approximately 1 μm, which can contribute to their permeability **(Figure 3-1b, d, f, and h)**; this is in agreement with the permeability results discussed above.

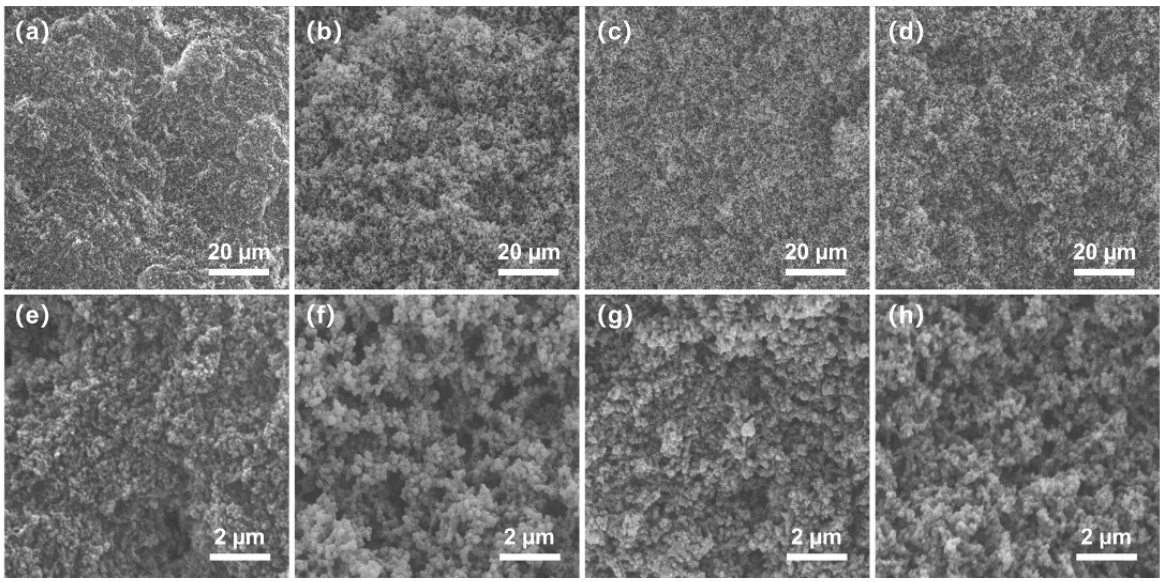

Figure 3-1. Scanning electron microscopy images of (a, e) monolith II, (b, f) monolith III, (c, g) monolith IV, and (d, h) monolith V. (a, b, c, and d) × 2000 magnification, (d, e, f, and g) × 10000 magnification.

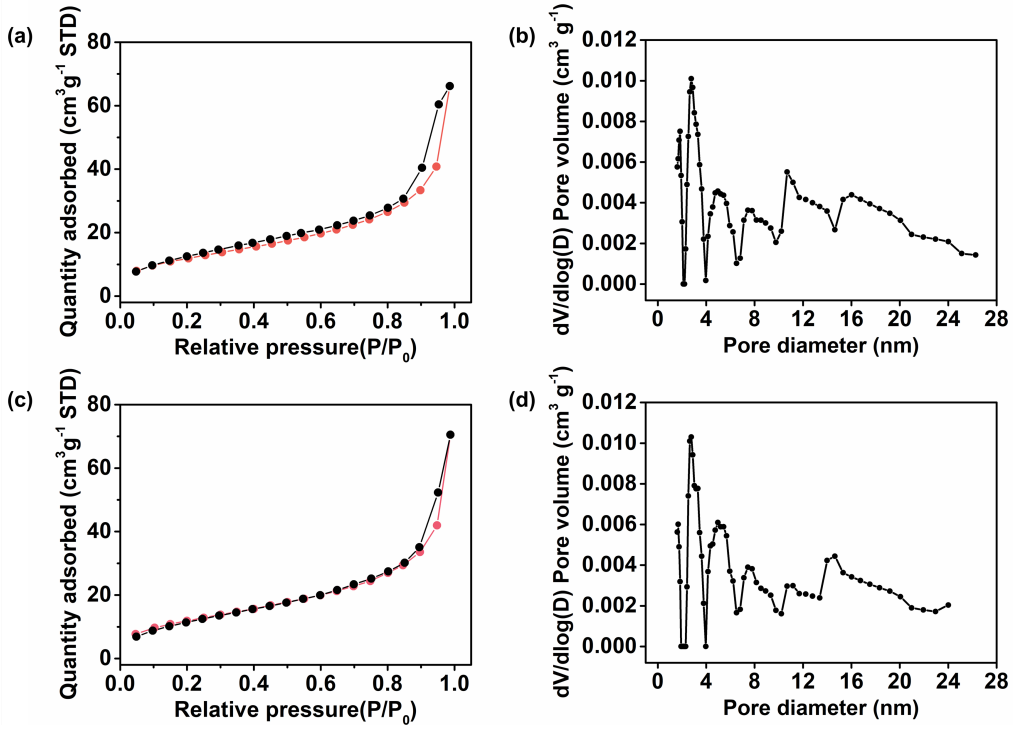

Figure 3-2. (a, c) Nitrogen adsorption/desorption isotherms and (b, d) corresponding pore size distribution plots of (a, b) monolith III and (c, d) monolith V, respectively.

On the other hand, nitrogen gas adsorption/desorption curves of the monoliths III and V were determined to evaluate their surface area and pore size distribution. From the results of nitrogen gas adsorption/desorption test, it could be attained that the surface areas of monolith III (**Figure 3-2a**) and monolith V (**Figure 3-2c**) were 43.2 m^2 g^{-1} and 44.0 m^2 g^{-1}, respectively.

Meanwhile, as observed from **Figure 3-2b** and **d**, the two monoliths exhibited a wider pore size distribution (3–25 nm)**,** indicating a presence of mesopores with different sizes. Thus, the permeability, SEM, and nitrogen gas adsorption/desorption results confirmed that the hierarchical porous structure was successfully formed in monoliths III and V. The presence of macropores facilitate the flow of liquid, while the mesopores provide a large surface area, exposing more functional groups on the skeleton surface of the monolith.

To confirm the chemical structure and composition of the prepared monoliths and study the introduction of the boronic acid group, *R*-M1 (its spectrum was the same as *S*-M1), M2, the crosslinking agent, monolith III, and monolith V were characterized using ATR-IR (**Figure 3-3**). The peaks at ~2120 cm^{-1} in the spectra of *R*-M1 (**Figure 3-3a**), M2 (**Figure 3-3b**), and the crosslinker (**Figure 3-3c**) can be assigned to the stretching vibrations of the C≡C bond. It was observed that the intensity of these peaks decreased and even disappeared in the spectra of monoliths III (**Figure 3-3d**) and V (**Figure 3-3e**), indicating that the polymerization between the C≡C bonds was successful. Additionally, the strong peaks at ~1650 cm^{-1} and ~1544 cm^{-1} in the spectra of *R*-M1 and M2 were attributed to the stretching vibrations of C=O and N−H bonds, respectively, which confirmed the presence of the amide group. The signals at 1339 and 862 cm^{-1} in M2 were ascribed to the characteristic peaks of the boronic group, and the strong peak at 1786 cm^{-1} in the spectra of the crosslinking agent was assigned to the stretching vibrations of the carboxyl group. These characteristic peaks were observed in the spectra of monoliths III and V, indicating that both the monomers and crosslinker sufficiently participated in the reaction. The ATR-IR results confirmed that the boronic group was

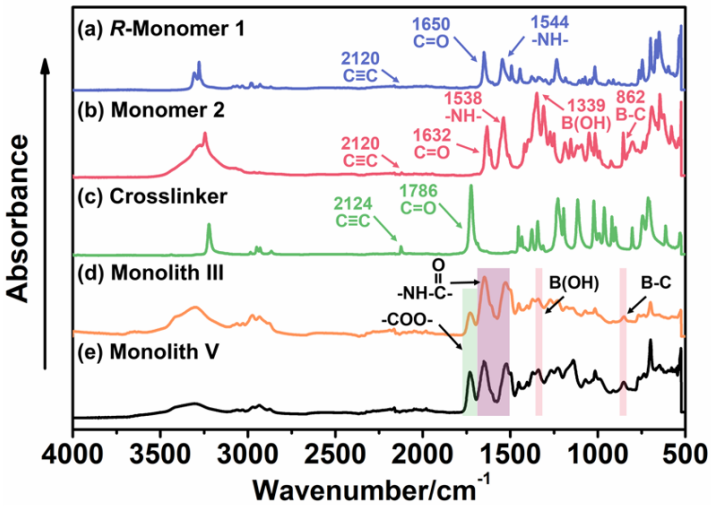

Figure 3-3. ATR/IR spectra of (a) chiral substituted acetylene (*R*-monomer 1), (b) achiral substituted acetylene (monomer 2), (c) crosslinker, (d) monolith III, and (e) monolith V.

successfully introduced into the materials, and the polymerization between the C≡C groups occurred during monolith formation.

Subsequently, monolith I (*R*-M1 and crosslinker), monolith III (*R*-M1, M2, and crosslinker), monolith V (*S*-M1, M2, and crosslinker), and monolith VI (M2 and crosslinker) were subjected to XPS to further characterize the chemical composition and investigate the successful introduction of boron on the surface of the monoliths after polymerization. As observed from the wide XPS spectra (**Figure 3-4a**), three elements (C, N, and O) were apparent on the surface of these four monoliths, while in the B 1s narrow spectra (**Figure 3-4b**), the characteristic signals of boron were observed in monoliths III, V, and VI, but not in monolith I (M2 was not added). The elemental atomic percentage (%) detected by XPS mesasurement on the surface of the monoliths is shown in **Table 3-2**, and the corresponding theoretical values is shown in **Table 3-3**. In **Table 3-2**, at higher M2 content in the pre-polymerization solution, the atomic percentage of boron in the monoliths also increased. In addition, monoliths III and V showed almost equal boron content, and the results dectect by XPS measurement is almost equal with theoretical values (**Table 3-3**). It suggested that the preparation method can be universally applied to enantiomers with different conformations. The above results implied that the boronic group could be successfully introduced as a functional group on the surface of the porous structure in the monoliths *via* the preparation method to recognize the compounds containing *cis*-diol groups *via* reversible covalent bonds.

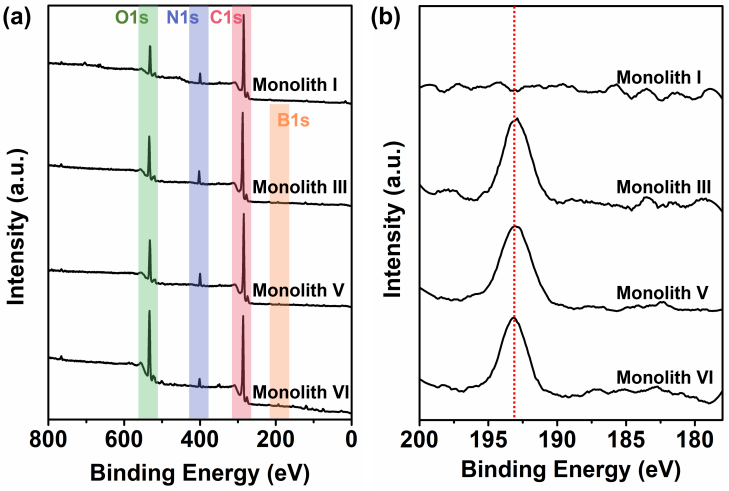

Figure 3-4. (a) Wide and (b) B 1s narrow X-ray photoelectron spectra of monoliths I, III, V, and VI.

TGA curves were collected to evaluate the thermal stability of the prepared monoliths III and V under nitrogen atmosphere. As observed from **Figure 3-5a**, there was significant weight loss from 216 to 600 ℃, and owing to the presence of boron, ~35% residual weight remained

(Figure 3-5a) in the two monoliths. This demonstrates that the monoliths possessed good thermal stability and the functional group was successfully introduced into the reaction system.

Table 3-2 The atomic percentage (%) on the surface of monoliths I, III, V and VI detected by X-ray photoelectron spectra.

	C	N	O	B
Monolith I	83.30	4.97	11.73	-
Monolith III	78.20	5.60	14.51	1.70
Monolith V	78.79	5.31	13.95	1.95
Monolith VI	71.27	3.61	22.10	3.02

Table 3-3 The theoretical atomic percentage (%) on the surface of monoliths I, III, V and VI.

	C	N	O	B
Monolith I	84.31	6.54	9.15	-
Monolith III	79.74	6.43	12.21	1.61
Monolith V	79.74	6.43	12.21	1.61
Monolith VI	66.87	6.13	20.85	6.13

The main chain of the substituted polyacetylene is a conjugated polyene structure with alternating single and double bonds, in which the C=C bond in the main chain shows *cis* and *trans* configurations whose content significantly affects the tacticity of the main chain in the polymer. To ensure high tacticity of the polymer main chain, $[(nbd)Rh^{+}B^{-}(C_6H_5)_4]$ was selected as the catalyst in this case, and Raman spectra was employed to investigate the *cis* and *trans* content in monoliths III and V. As observed from **Figure 3-5b**, strong signals of *cis* C=C and C−C were observed at 1623 and 1336 cm^{-1}, respectively, whereas the signals of *trans* C=C at 1431 cm^{-1} and C−C at 1213 cm^{-1} were very weak. This suggests that the main chain of the copolymer in monoliths III and V exhibited a higher *cis* content and tacticity, which facilitated the formation of the helical structure.

As previous literature reported,[33] substituted polyacetylene synthesized by chiral substituted acetylene can form a helical conformation with single excess rotation due to conjugated structure of the main chain, which manifests optical activity. Conversely, achiral substituted acetylene without the chiral center easily forms substituted polyacetylene with a racemic helix conformation, with no optical activity. In this study, it was expected to fabricate a monolith that possess not only optical activity but also functional group, and thus chiral

substituted polyacetylene (*R*- or *S*-M1) and achiral substituted polyacetylene (M2) with the phenylboronic acid group were selected. To verify whether the prepared monoliths exhibited optical activity, the CD and UV–vis absorption spectra were employed to investigate them. Because the monoliths cannot be dissolved using a common solvent, the mixture of the monoliths and KBr was compressed into tablets for qualitative measurements. As illustrated in **Figure 3-5c**, the negative signals near 400 nm appeared in the CD spectra of monolith I (prepared by *R*-M1 and crosslinker) and III (prepared by *R*-M1, M2 and crosslinker), while the positive signal at the same position appeared in monolith V (prepared by *S*-M1, M2 and crosslinker). However, there is no signal in the CD spectrum of monolith VI (prepared by M2 and crosslinker), indicating that the helical conformation with single excess rotation did not form owing to the absence of the chiral center. Moreover, the adsorption peaks also appeared at the corresponding positions in the UV–vis absorption spectra of monoliths I, III, and V as observed from **Figure 3-5d**. These results demonstrated that the different one-handed helical conformations respectively present in the monoliths III and V, which exhibited good optical activity even when achiral M2 participated in the polymerization with M1 to fabricate the copolymer.

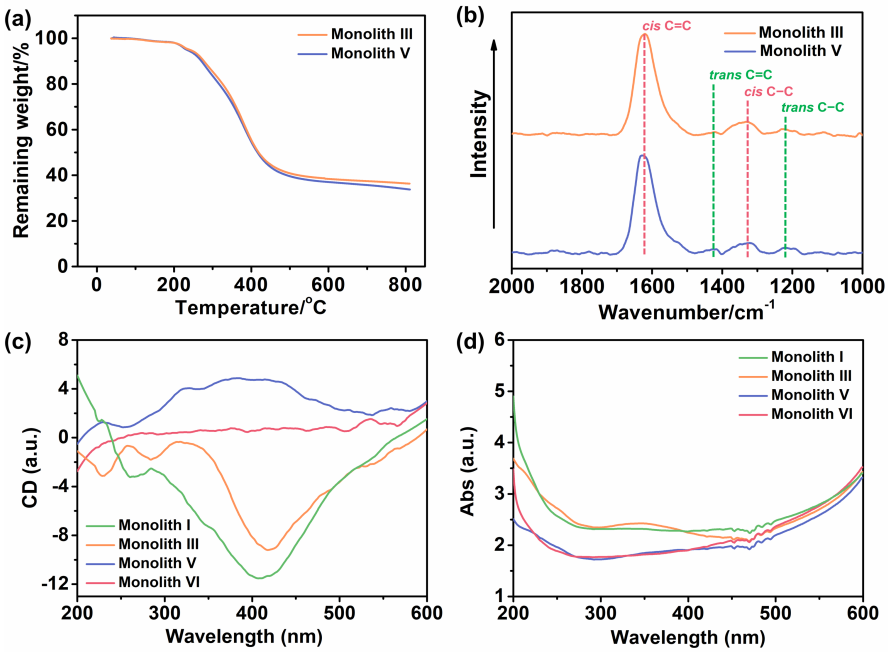

Figure 3-5. (a) Thermogravimetric analysis (TGA) curves of monoliths III and V. With a scanning rate of 10 °C min^{-1}, all the TGA curves were collected under a nitrogen atmosphere. (b) Raman spectra of monoliths III and V with the 532 nm excitation wavelength. (c) Circular dichroism (CD) and (d) ultraviolet–visible (UV−vis) absorption spectra of monoliths I, III, V and VI. The monoliths were respectively combined with KBr to compress into tablets to determine their spectra at 25 °C.

3.3.3 Investigation for selectively chiral adsorption ability of monoliths

As above mentioned, the resulting monoliths simultaneously possessed chirality and boronic acid group, indicating that they may show selectivity for the target compound with chirality and *cis*-diol group. α-Glucose has *cis*-diol group, and thus it could be adsorbed by the materials with boronic acid group to form reversible covalent bonds. Moreover, α-glucose has two conformations including α-D- and α-L-glucose, which can interact with chiral materials, such as helical polymer. Therefore, the pair of enantiomers was chosen to investigate the selectively chiral adsorption ability of the resulting monoliths. The contact angle test was used to determine contact angle of three different solutions (PB solution (pH=8.6), 10 mg mL^{-1} α-D-glucose PB solution, and 10 mg mL^{-1} α-L-glucose PB solution) on monoliths III and V. As observed from **Figure 3-6a** and **d**, the PB solution contact angles on monoliths III (prepared by *R*-M1, M2 and crosslinker) and V (prepared by *S*-M1, M2 and crosslinker) were respectively 136°±2° and 131°±2°. However, when the 10 mg mL^{-1} α-D- and α-L-glucose PB solutions were used as samples, the values of contact angles on the two monoliths were decreased. The possible reason is the existence of boronic acid group. Even more to the point, α-D-glucose PB solution contact angle on monolith III was 126°±1° in **Figure 3-6b**, which was higher than that of α-L-glucose PB solution (113°±1°) in **Figure 3-6c**. On the contrary, α-D-glucose PB solution contact angle on monolith V was 109°±2° (**Figure 3-6e**), and α-L-glucose PB solution contact angle increased to 128°±2° in (**Figure 3-6f**). The phenomena implied that monolith III has stronger interaction with α-L-glucose compared to α-D-glucose

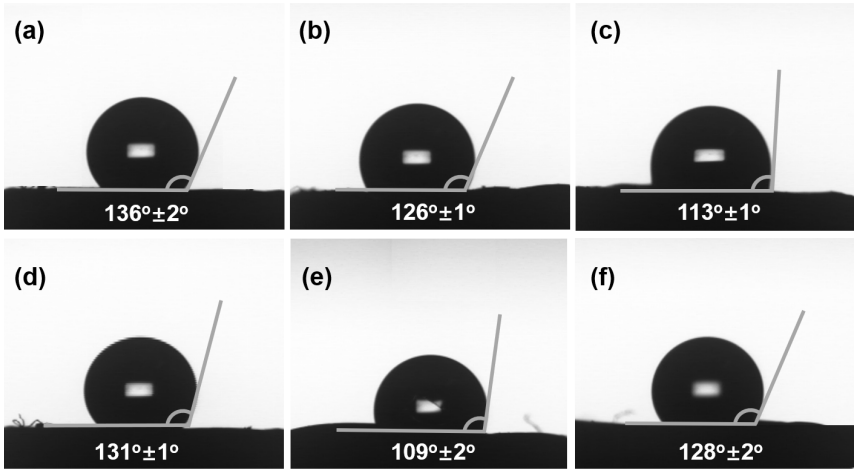

Figure 3-6. PB solution (pH=8.6) contact angle on the surface of (a) monolith III and (d) monolith V. Ten mg mL^{-1} α-D-glucose PB solution contact angle on the surface of (b) monolith III and (e) monolith V. Ten mg mL^{-1} α-L-glucose PB solution contact angle on the surface of (c) monolith III and (f) monolith V.

owing to matching chiral conformation, and monolith V showed a opposite performance. It could be demonstrated that the synthesized monoliths have recognition ability for α-glucose with different conformation.

Meanwhile, 0.5 mg mL^{-1} α-D- and α-L-glucose PB solution (pH=8.6) were chosen to investigate the selectively chiral adsorption ability of the resulting monoliths. The water contact angle test was used to determine the change in water contact angle of monoliths before and after adsorbing α-D- and α-L-glucose. In **Figure 3-7**, it can be found that the water contact angles of monoliths III and V were greater than 120°, indicating that they are hydrophobic. After adsorbing α-D- and α-L-glucose, the water contact angles of monolith III respectively decreased to 75°±3° (**Figure 3-7b**) and 43°±2° (**Figure 3-7c**), and monolith V respectively changed to 39°±2° (**Figure 3-7e**) and 47°±3° (**Figure 3-7f**). It indicated that more amount of α-L-glucose was adsorbed on the surface of monolith III compared to α-D-glucose, and more amount of α-D-glucose was adsorbed on the surface of monolith V in the same condition. These results could prove that the synthesized monoliths have selectively chiral adsorption ability for the target compound with chirality and *cis*-diol group and the potential in chiral separation or adsorption.

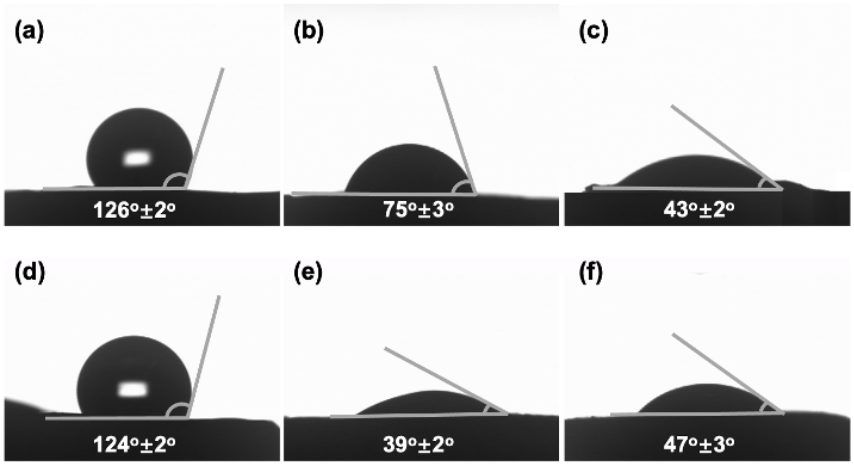

Figure 3-7. Water contact angle of the surface of (a) pristine, (b) adsorbed α-D-glucose, and (f) adsorbed α-L-glucose monolith III, and (d) pristine, (e) adsorbed α-D-glucose, and (f) adsorbed α-L-glucose monolith V.

3.4 Conclusions

Using the CPIPS method, hierarchically porous boronic acid group-functionalized monoliths with optical activity were successfully synthesized. Chiral substituted acetylene and achiral substituted acetylene with the boronic acid functional group were used as monomers in the presence of a catalyst ([(nbd)$Rh^{+}B^{-}(C_6H_5)_4$]), crosslinker, and porogenic solvent (THF and CH_3OH). The macropores size could be regulated by changing the composition of the pre-polymerization solution. Moreover, analysis by SEM and nitrogen gas adsorption/desorption isotherms indicated that the monoliths possessed a large surface area and hierarchical porous structure. Further, ATR-IR and XPS spectra confirmed that the boronic acid functional group was successful introduced on the surface of the porous structure in the resulting monolith. Furthermore, TGA confirmed that the monoliths were thermally stable. Most importantly, the polymerization occurred in the substituted acetylene and was initiated by the rhodium catalyst; thus, the main chain of the copolymer that constituted the monoliths showed a high *cis* content, as per Raman spectra, indicating a high tacticity. In the case where both the enantiomers (*R*-M1 and *S*-M2) were used as monomers, reverse signals in the CD spectra derived from the formation of the chiral helical substituted polyacetylene were observed, revealing that the monoliths had good optical activity. The optical activity and boronic acid functional group in the monolith can interact with target compound with chirality and *cis*-diol group. These results clearly indicate that the monoliths have the potential for various applications, such as chiral recognition, chiral controlled release, and selectively chiral adsorption.

3.5 References

1. V. Yesilyurt, M. J. Webber, E. A. Appel, C. Godwin, R. Langer, D. G. Anderson, *Adv. Mater.* 2016, **28**, 86–91.
2. P. Shen, Y. Xia, *Anal. Chem.* 2014, **86**, 5323–5329.
3. R. Ma, L. Shi, *Polym. Chem.* 2014, **5**, 1503–1518.
4. T. James, K. Sandanayake, S. Shinkai, *Angew. Chem. Int. Ed.* 1996, **35**, 1910–1922.
5. T. Lan, Q. Guo, *Nanotechnol. Rev.* 2019, **8**, 548–561.
6. D. Li, Y. Chen, Z. Liu, *Chem. Soc. Rev.* 2015, **44**, 8097–8123.
7. X. Dou, N. Mehwish, C. Zhao, J. Liu, C. Xing, C. Feng, *Acc. Chem. Res.* 2020, **53**, 852–862.
8. P. Etayo, A. Vidal-Ferran, *Chem. Soc. Rev.* 2013, **42**, 728–754.
9. P. Xing, Y. Zhao, *Acc. Chem. Res.* 2018, **51**, 2324–2334.
10. E. Tokunaga, T. Yamamoto, E. Ito, N. Shibata, *Sci. Rep.* 2018, **8**, 17131.
11. E. Yashima, N. Ousaka, D. Taura, K. Shimomura, T. Ikai, K. Maeda, *Chem. Rev.* 2016, **116**, 13752–13990.
12. S. Wang, D. Hu, X. Guan, S. Cai, G. Shi, Z. Shuai, J. Zhang, Q. Peng, X. Wan, *Angew. Chem. Int. Ed.* 2021, **60**, 21918–21926.
13. P. Li, J. Deng, *Advanced Functional Materials* 2021, **31**, 2105315.
14. Y. Gu, L. Liu, Y. Wang, C. Zhang, H. Dong, T. Aoki, *Macromolecules* 2021, **54**, 10216–10223.
15. K. Shimomura, T. Ikai, S. Kanoh, E. Yashima, K. Maeda, *Nat. Chem.* 2014, **6**, 429–434.
16. B. Zhao, J. Deng, *Polym. Rev.* 2016, **57**, 119–137.
17. M. Núñez-Martínez, S. Arias, E. Quiñoá, R. Riguera, F. Freire, *Chem. Mater.* 2021, **33**, 4805–4812.
18. B. Zhao, J. Deng, J. Deng. *Macromol. Rapid Commun.* 2016, **37**, 568–574.
19. K. Zhou, L. Tong, J. Deng, W. Yang, *J. Mater. Chem.* 2010, **20**, 781–789.

20. D. Liu, L. Zhang, M. Li, W. Yang, J. Deng, *Macromol Rapid Commun* 2012, **33**, 672–677.
21. J. Liang, Y. Wu, J. Deng, *ACS Appl. Mater. Interfaces* 2016, **8**, 12494–12503.
22. D. Zhang, C. Song, J. Deng, W. Yang, *Macromolecules* 2012, **45**, 7329–7338.
23. S. Ma, L. Zhang, S. Wang, H. Zhang, X. You, J. Ou, M. Ye, Y. Wei, *Anal. Chim. Acta* 2019, **1058**, 97–106.
24. C. M. Parlett, K. Wilson, A. F. Lee, *Chem. Soc. Rev.* 2013, **42**, 3876–3893.
25. I. Nischang, T. J. Causon, *TrAC, Trends Anal. Chem.* 2016, **75**, 108–117.
26. G. Hasegawa, K. Morisato, K. Kanamori, K. Nakanishi, *J. Sep. Sci.* 2011, **34**, 3004–3010.
27. B. Fang, M. Kim, S.-Q. Fan, J. H. Kim, D. P. Wilkinson, J. Ko, J.-S. Yu, *J. Mater. Chem.* 2011, **21**, 8742–8748.
28. Y. S. Hu, P. Adelhelm, B. M. Smarsly, S. Hore, M. Antonietti, J. Maier, *Adv. Funct. Mater.* 2007, **17**, 1873–1878.
29. J. Lin, H. Huang, M. Wang, J. Deng, *Polymer Chemistry* 2016, **7**, 1675–1681.
30. X. Deng, J. Liang, J. Deng, *Chem. Eng. J.* 2016, **306**, 1162–1171.
31. R. Nomura, K. Yamada, J. Tabei, Y. Takakura, T. Takigawa, T. Masuda, *Macromolecules* 2003, **36**, 6939–6941.
32. B. Chen, J. Deng, W. Yang, *Adv. Funct. Mater.* 2011, **21**, 2345–2350.
33. Y. Wang, L. Zhang, T. A. Asoh, H. Uyama, *ACS Appl. Mater. Interfaces* 2021, **13**, 48020–48029.
34. L. Wu, Y. Li, Z. Fu, B. L. Su, *Natl. Sci. Rev.* 2020, **7**, 1667–1701.
35. M. H. Sun, S. Z. Huang, L. H. Chen, Y. Li, X. Y. Yang, Z. Y. Yuan, B. L. Su, *Chem. Soc. Rev.* 2016, **45**, 3479–3563.

Concluding Remarks

In this doctoral dissertation, different types of hierarchically porous monoliths were synthesized *via* phase separation including TIPS and CIPS. The prepared monoliths had a homogenous porous structure, and simultaneously contained two or more pore sizes. Most importantly, it could be confirmed that they exhibited good pofermance in various applications.

In Chapter 1, a cost-effective and facile method was developed for the fabrication of PI and hybrid PI (PI-*co*-POSS) monoliths, in which the shortcomings of the traditional method in porous PI materials could be overcome, such as complicated preparation process and high cost from supercritical drying. After physical chacterizations, it could proved that the prepared PI-based monoliths possessed great thermal stability, good hydrophilicity, high mechanical strength, and hierarchically porous structure. As the results, they was applied in oil–water separation, in which the resulting hybrid PI monoliths with stronger hydrohilicity and lower density exhibited better adsorption performance for organic solvents and silicone oil than pure PI monolith. In addition, the surface of POSS-epoxy hybridized PI (PI-*co*-POSS) monolith can be modified into a hydrophilic layer by reaction between the hydrophilic polymer and epoxy groups exposed on the surface. This demenstrates that PI-*co*-POSS monoliths have potential in liquid diode application to achieve oil–water separation.

In Chapter 2, a flexible and highly efficient one-step method was developed to fabricate chiral hierarchical porous monoliths *via* CIPS using substituted acetylene and crosslinker in the presence of porogenic solvent (tetrahydrofuran and methanol) in which the complex doping and complicated procedures were not required. The resulting monoliths directly constructed by chiral substituted acetylene exhibited good optical activity owing to the orderly helical structure in the main chain. Morover, the hierarchical pore structure with through-pore and high surface area existed in the monoliths, which provides more active sites and space for interaction between monolithic materials and the solution. Therefore, the hierarchically porous monoliths with optical activity was used to obtain enantiomer with one conformation from the supersaturated racemic solition of Boc-alanine in enantioselective crystallization. The induced

crystals by the prepared monoliths showed high *e.e*. values, inadicating that the monoliths have application potential in enantioselective crystallization.

In Chapter 3, to further develop the “one step” method in Chapter 2 and borden its feasibility, hierarchically porous boronic acid group-functionalized monoliths with optical activity were fabricated using the “one step” method. As shown in the results of chacterizations, the resulting functionalized hierarchically porous monoliths, which were constrcuted by chiral substituted acetylene with chiral site and achiral substituted acetylene with a boronic acid group, possessed not only hierarchically porous structure, large surface area but also boronic acid group, high tacticity, and optical activity. As the results, the prepared monoliths may have potential in selective recognition ability for the target compouns with chirality and *cis*-diol group. Afterwards, as confirmed by contact angle test, the prepared monoliths were successfully used in selective recognition ability for α-glucose, demonstrating that they had potential in recognition, separation, and adsorption of compound with chirality and *cis*-diol groups.

In summary, the strategies on the fabrication of monoliths with hierarchically porous structure were developed in the dissertation. In the future, other types of monoliths with hierarchically porous structure could be prepared *via* phase separation including TIPS and CIPS by means of monomers with different functional group to improve their physical and chemical properties and broaden their field of application.

List of Publications

1. Hydrophobic and hydrophilic modification of hierarchically porous monolithic polyimide derivatives as functional liquid absorbers

Yan Wang, Luwei Zhang, Taka-Aki Asoh*, Hiroshi Uyama*

Materials Advances, 2021, **2**, 3560–3568.

2. Facile preparation of hierarchically porous monolith with optical activity based on helical substituted polyacetylene *via* one-step synthesis for enantioselective crystallization

Yan Wang, Luwei Zhang, Taka-Aki Asoh*, Hiroshi Uyama*

ACS Applied Materials & Interfaces, 2021, **13**, 48020–48029.

3. Facile fabrication of hierarchically porous boronic acid group-functionalized monoliths with optical activity for recognizing glucose with different conformation

Yan Wang, Luwei Zhang, Yu-I Hsu*, Taka-Aki Asoh, Hiroshi Uyama*

Frontiers in Chemistry, 2022, **10**, 939368.

Acknowledgments

This study was carried out from 2019 to 2022 at Department of Applied Chemistry, Graduate School of Engineering, Osaka University. During these three years, I received a lot of support from many nice people.

First and foremost, I would like to express my deepest appreciation to my supervisor, Prof. Hiroshi Uyama. I am very thankful to him for giving me opportunity to study at Osaka University. I learned a lot from his continuous guidance, warm encouragement, and suggestions. This thesis would not have been possible without his support and help. His warm laughter accompanied me through the happy three years, and I feel very lucky to be his student. Besides my supervisor, I would like to thank Prof. Hidehiro Sakurai and Prof. Takahiro Kozawa for their suggestions and help in my experiments and scientific paper writing. I learned a lot during the discussion with them.

I also want to express my profoundly gratitude to Prof. Taka-Aki Asoh, for his experience sharing, suggestions, and inspiration in my research. He always gives me the fastest feedback in submitting and revising manuscripts. As long as the status of my article is updated, I can immediately receive the related email from him, whether it is early morning or late at night.

I appreciate Assoc. Prof. Yu-I Hsu for her kind help and expert suggestions to improve the quality of my research. I am grateful to Assist. Prof. Akihide Sugawara to revise my doctoral abstract and defense slides. Thank you for giving us wonderful memories in amazing park and bringing us to eat the most delicious yakiniku.

I really appreciate Ms. Yoko Uenishi and Ms. Tomoko Shimizu for their kind help and care during these three years. I am very thankful to the support of past and present members in Uyama Lab: Dr. Yasushi Takeuchi, Dr. Xinnan Cui, Dr. Chen Qian, Dr. Toshiki Tamiya, Dr. Shunsuke Mizuno, Dr. Naharullah Bin Jamaluddin, Dr. Raghav Soni, Mr. Mark Adam Malaluan Ferry, Mr. Yuxiang Jia, Ms. Juan Wang, Mr. Peng Du, Mr. Kazuki Shibasaki, Ms. Linxuan Li, Ms. Zeying Cao, Ms. Xunran Guo, Ms. Jiaxin Chen, Ms. Ying Yao, Ms. Guan Wang, Mr. Toshiki Honda, Ms. Airi Ozaki, Mr. Yuya Fujiwara, Mr. Atsushi Koizumi, Ms. Yuka Kashihara, Mr. Yuji Kiba, Mr. Takeshi Hiraoka, Mr. Yuki Shioji, Mr. Nontarin Roopsung, Mr. Emil Hajili, Ms. Madhurangika Panchabashini Horathal Pedige, Ms. May Myat Noe, Ms. Hasinah Binti Mohamed Rafiq, Ms. Judit Rebeka Molnar, Ms. Izzah Durrati Binti Haji Abdul Hamid, Ms.

Sooyeon Noh, Ms. Thuy Le Huynh An, Mr. Motoi Oda, Ms. Suzune Miki, Mr. Kaita Kikuchi, Mr. Koki Tsujita, Mr. Hajime Fujimori, Ms. Rika Onishi, Mr. Shotaro Yano, Ms. Rina Kugimiya, Ms. Kyoko Tanimura, Ms. Chikabo Abe, Ms. Erina Katsuragawa, Mr. Yasushi Takeuchi, Mr. Atsuki Takagi and etc. for their kind-hearted help in my lab and daily life.

I would like to thank Dr. Bozhi Chen, Dr. Yankun Jia, Dr. Zhengtian Xie, Dr. Haomin Yan, Dr. Hanyu Wen, Dr. Yanting Lyu, Ms. Meng Wei, Mr. Junyi Han and Ms. Manjie He. I obainted a lot of beautiful memories with you in Japan, such as Lake Biwa, Shikoku, Okinawa, Kyoto, Tokyo, Hokkaido and Wakayama… I hope everything goes well for you.

I would like to express appreciation to my parents, my parents-in-law, my brother, and my best friends Ji Xiaoyu and Shi Fan. They always give me countless love and endless support, ane I love them so much. I would like to thank my husband Luwei Zhang for his company, love, and encouragement. I feel so happy to be your wife, and life with you is with great happiness. We are the best partners in research and life (besides badminton doubles match), and overcame one difficulty after another together. I wish we can become great researchers in the future.

Finally, I always appreciate the China Scholarship Council for the constant support during these three years. I am grateful to my country for giving me a chance to study in Japan without any monetary burden. I will show my gratitude toward my country by contributing the cutting-edge research and sharing my experience.

WANG YAN

June 2022

Suita, Osaka, Japan